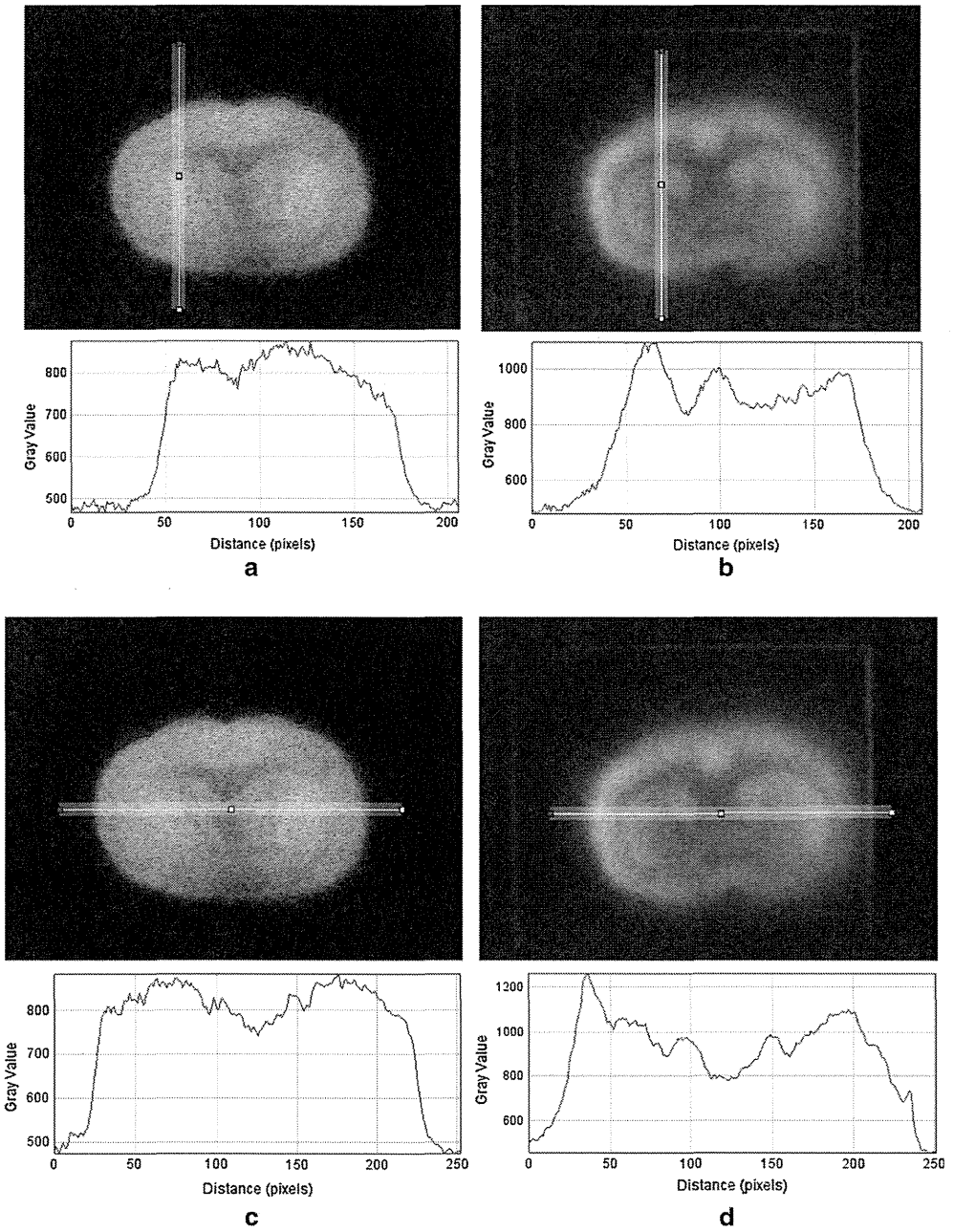

Fig. 16 *Vertical direction* profiles of Cerenkov-light image (**a**), positron image with CWO scintillator (**b**), *horizontal direction* profiles of Cerenkov-light image (**c**), and positron image with CWO scintillator (**d**)

the position distribution for Cerenkov-light images. However, the ultrahigh resolution of Cerenkov-light imaging will be useful at least for transparent subjects including phantom studies.

Acknowledgments This work was partly supported by the Japan Science and Technology Association and Ministry of Education, Science, Sports and Culture, Japan.

References

1. Robertson R, Germanos MS, Li C, Mitchell GS, Cherry SR, Silva MD. Optical imaging of Cerenkov light generation from positron-emitting radiotracers. Phys Med Biol. 2009;54:N355–65.
2. Spinelli AE, D'Ambrosio D, Calderan L, Marengo M, Sbarbati A, Boschi F. Cerenkov radiation allows in vivo optical imaging of positron emitting radiotracers. Phys Med Biol. 2010;55:483–95.
3. Knoll G. Radiation detection and measurement. 3rd ed.

4. Cho JS, Taschereau R, Olma S, Liu K, Chen YC, Shen CK, et al. Cerenkov radiation imaging as a method for quantitative measurements of beta particles in a microfluidic chip. Phys Med Biol. 2009;54:6757–71.
5. Liu H, Ren G, Miao Z, Zhang X, Tang X, Han P, et al. Molecular optical imaging with radioactive probes. PLoS ONE. 2010;5: e9470.
6. Liu H, Ren G, Liu S, Zhang X, Chen L, Han P, et al. Optical imaging of reporter gene expression using a positron-emission-tomography probe. J Biomed Opt. 2010;15:060505.
7. Ruggiero A, Holland JP, Lewis JS, Grimm J. Cerenkov luminescence imaging of medical isotopes. J Nucl Med. 2010;51: 1123–30.
8. Park JC, Il An G, Park SI, Oh J, Kim HJ, Su Ha Y, et al. Luminescence imaging using radionuclides: a potential application in molecular imaging. Nucl Med Biol. 2011;38(3):321–9.
9. Hu Z, Liang J, Yang W, Fan W, Li C, Ma X, et al. Experimental Cerenkov luminescence tomography of the mouse model with SPECT imaging validation. Opt Expr. 2010;18:24441–50.
10. Park JC, Yu MK, An GI, Park SI, Oh J, Kim HJ, et al. Facile preparation of a hybrid nanoprobe for triple-modality optical/PET/MR imaging. Small. 2010;6:2863–8.
11. Boschi F, Calderan L, D'Ambrosio D, Marengo M, Fenzi A, Calandrino R, et al. In vivo 18F-FDG tumour uptake measurements in small animals using Cerenkov radiation. Eur J Nucl Med Mol Imaging. 2011;38:120–7.
12. Xu Y, Liu H, Cheng Z. Harnessing the power of radionuclides for optical imaging: Cerenkov luminescence imaging. J Nucl Med. 2011;52(12):2009–18.
13. Elrick RH, Parker RP. The use of Cerenkov radiation in the measurement of betaemitting radionuclides. Int J Appl Radiat Isot. 1968;19:263–71.
14. Jelley JV. Cerenkov radiation and its applications. Br J Appl Phys. 1955;6:227–32.
15. Rasband, WS, ImageJ, US National Institutes of Health, Bethesda, MD, USA. 1997–2012. http://imagej.nih.gov/ij/.
16. Schneider CA, Rasband WS, Eliceiri KW. NIH Image to ImageJ: 25 years of image analysis. Nat Methods. 2012;9:671–5.
17. Constantinescu CC, Mukherjee J. Performance evaluation of an Inveon PET preclinical scanner. Phys Med Biol. 2009;54(9): 2885–99.
18. Yamamoto S, Watabe H, Kanai Y, Watabe T, Kato K, Hatazawa J. Development of an ultrahigh resolution Si-PM based PET system for small animals. Phys Med Biol. 2013;58(21):7875–88.

Bioorganic & Medicinal Chemistry 22 (2014) 2563–2570

Contents lists available at ScienceDirect

Bioorganic & Medicinal Chemistry

journal homepage: www.elsevier.com/locate/bmc

Selective accumulation of [^{62}Zn]-labeled glycoconjugated porphyrins as multi-functional positron emission tomography tracers in cancer cells

Masato Tamura [a], Hirofumi Matsui [a,*], Shiho Hirohara [b,c], Kiyomi Kakiuchi [c], Masao Tanihara [c], Naruto Takahashi [d], Kozi Nakai [d], Yasukazu Kanai [e], Hiroshi Watabe [e], Jun Hatazawa [f,g]

[a] Graduate School of Comprehensive Human Sciences, University of Tsukuba, 1-1-1 Ten-noudai, Tsukuba, Ibaraki 305-8573, Japan
[b] Department of Chemical and Biological Engineering, Ube National College of Technology, 2-14-1 Tokiwadai, Ube 755-8555, Japan
[c] Graduate School of Materials Science, Nara Institute of Science and Technology (NAIST), Ikoma, Nara 630-0192, Japan
[d] Graduate School of Science, Osaka University, Toyonaka, Osaka 560-0043, Japan
[e] Department of Molecular Imaging in Medicine, Osaka University Graduate School of Medicine, 2-2 Yamadaoka, Suita-city, Osaka 565-0871, Japan
[f] Department of Nuclear Medicine and Tracer Kinetics, Osaka University Graduate School of Medicine, 2-2 Yamadaoka, Suita-city, Osaka 565-0871, Japan
[g] Department of Nuclear Medicine, WPI Immunology Frontier Research Center, 2-2 Yamadaoka, Suita-city, Osaka 565-0871, Japan

ARTICLE INFO

Article history:
Received 26 December 2013
Revised 14 February 2014
Accepted 14 February 2014
Available online 1 March 2014

Keywords:
Positron emission tomography
[^{62}Zn]-labeling PET tracer
[^{62}Zn]-zinc porphyrins
Cancer selective accumulation

ABSTRACT

Positron-emission tomography (PET) can be used to visualize active stage cancer. Fluorine-18 ([^{18}F])-labeled 2-([^{18}F])2-deoxy-2-fluoroglucose (([^{18}F])-FDG), which accumulates in glucose-dependent tissues, is a good cancer-targeting tracer. However, ([^{18}F])-FDG is obscured in glucose-dependent normal tissues. In this study, we assessed the cancer-selective accumulation of zinc-labeled glycoconjugated 5,10,15, 20-tetrakis(pentafluorophenyl)porphyrin (ZnGlc**1**–**4**), both in vitro and in vivo. Experiments using both normal and cancer cells confirmed the relationship between cancer cell-selective accumulation and the substitution numbers and orientations of glycoconjugated porphyrins. ZnGlc*trans*-**2** accumulated at greater levels in cancer cells compared with other glycoconjugated porphyrins. PET imaging showed that ZnGlc*trans*-**2** accumulated in tumor.

1. Introduction

Positron-emission tomography (PET) can be used to visualize the properties of cancer. PET images can provide important information and are especially helpful in the detection of the active stage of cancer cells and in developing a treatment strategy. The PET tracer fluorine-18 ([^{18}F]) ($t_{1/2}$ = 110 min)-labeled 2-([^{18}F])2-deoxy-2-fluoroglucose (([^{18}F])-FDG)[1] is a good cancer-targeting tracer, which accumulates in glucose-dependent tissues. However, ([^{18}F])-FDG is obscured in glucose-dependent normal tissues such as the brain and, therefore, it is limited to low glucose-dependent tissues. In addition, cancer does not always require glucose. An existing problem is that the kinds of PET tracers cannot be chosen on a case-by-case basis because there are few PET tracers. Thus, different metabolic ([^{18}F])-labeled PET tracers derived from glucose metabolism have been required and are being developed. For example, cationic charge polymers,[2] folate,[3] and gold-nanoparticles[4] are used as PET tracers. Bombesin analogues selectively accumulated in a gastrin-releasing peptide receptor (GRPR)-expressing tumor in vitro and in vivo,[5] suggesting that the chemicals of cancer-selective accumulation in vitro remain distributed in tissues throughout the body.

Gallium-68 ([^{68}Ga]) and zinc-62 ([^{62}Zn]) were used as radiolabeling-nuclides for PET.[6] ([^{18}F])-labeled PET tracers are required for fast ([^{18}F])-labeling methods because of the short half-life of ([^{18}F]) ($t_{1/2}$ = 110 min).[7] When more than 6 h of half-life is needed to perform PET tracing in a clinical laboratory,[8] the radioactivity should be eliminated after PET imaging to prevent radiation exposure. Thus, an ideal PET tracer has a short half-life or biological half-life of several hours. It is also better to choose the radioactive metal based on toxicity to avoid unexpected side effects. For example, a [^{68}Ga]-labeled PET tracer induces nephrogenic systemic fibrosis[9] by blocking ion channels[10] when the gadolinium ion is released from the tracer or exists as a residue. The toxicity of the [^{62}Zn] ion is not problematic for use in clinical PET[11,12] and has

Abbreviations: PET, positron-emission tomography; H_2Glc**1**–**4**, bisglycoconjugated porphyrins; ZnGlc**1**–**4**, [^{62}Zn]-labeled bisglycoconjugated porphyrins.

* Corresponding author. Tel.: +81 29 853 3466; fax: +81 29 853 3218.
E-mail address: hmatsui@md.tsukuba.ac.jp (H. Matsui).

http://dx.doi.org/10.1016/j.bmc.2014.02.021
0968-0896/

an adequate half-life of approximately 9 h. Thus, we incorporated the [^{62}Zn] ion into a PET tracer.

In an attempt to overcome the limitations to PET through safe and photodynamic therapy (PDT) applications, we reported a multi-functional PET tracer of porphyrin-based chemicals based on PDT agents of glycoconjugated porphyrins, namely perfluorophenylporphyrin, which has *S*-glucopyranosyl groups (H_2Glc**1**–**4**).[13] While the PDT tracers caused visual side effects in vitro, more photocytotoxicity was observed at certain drug concentrations. The cellular uptake of H_2Glc**1**–**4** differed based on the numbers of *S*-glycosylated groups and orientations (*cis* or *trans*); in order of increasing cellular uptake were H_2Glc**1**, H_2Glc**4**, H_2Glc*cis*-**2**, H_2Glc**3**, and H_2Glc*trans*-**2**.[13] The amount of cellular uptake was related to photocytotoxicity.[13] In our previous study, we reported the possibility of [^{62}Zn]-labeled bisglycoconjugated porphyrins, namely [^{62}Zn]-labeled ZnGlc*cis*-**2** ([^{62}Zn]-ZnGlc*cis*-**2**) and [^{62}Zn]-labeled ZnGlc*trans*-**2** ([^{62}Zn]-ZnGlc*cis*-**2**), as PET agents. [^{62}Zn]-labeling containing a porphyrin ring could be achieved within 30 min, and the signals of [^{62}Zn]-ZnGlc*cis*-**2** and [^{62}Zn]-ZnGlc*trans*-**2** were detected by PET in tumor-bearing mice, without any visible side effect in vivo.[14] In addition, photocytotoxicity of non-radioactive zinc ([Zn])-ZnGlc*cis*-**2** and [Zn]-ZnGlc*trans*-**2** showed cellular uptake similar to that of H_2Glc*cis*-**2** and H_2Glc*trans*-**2**.[14]

Cancer-selective accumulation is an important consideration for PET tracers. To clarify the cancer-selective effects of PET tracers, rat gastric mucosal epithelial cells (RGM-1)[15] and oncogenic RGM-1 mutated cells (RGK-1)[16], were used in this study. RGK-1 was established from RGM-1 through exposure to the carcinogenic substance *N*-methyl-*N*′-nitro-*N*-nitrosoguanidine.[16] Thus, RGM-1 and RGK-1 have the same genetic background, which can reveal differences between the properties of normal cells and cancerous cells.[17] In RGK-1 cells, the expression of heme carrier protein 1 (HCP1), which transports porphyrin-based chemicals into cells,[18] is obviously higher than that in RGM-1 cells. As a result, the uptake of porphyrin derivatives in RGK-1 cells is enhanced.[18] We have already reported that RGK-1 was preferentially injured by PDT with [Zn]-ZnGlc*cis*-**2** or [Zn]-ZnGlc*trans*-**2** in vitro.[14] However, cancer cell-selective accumulation and tissue distribution had not been confirmed.

In this study, we assessed the in vitro and in vivo cancer-selective accumulation of Zn laserphyrin® and ZnGlc**1**-**4** (Scheme 1). Cell experiments using both RGM-1 and RGK-1 have confirmed the relationship between cancer cell-selective accumulation and the substitution numbers or orientations (*cis* or *trans*) of glycoconjugated porphyrins. Animal studies revealed the tissue distribution of the porphyrins by anatomy and PET/MRI imaging.

2. Materials and methods

2.1. Materials

Ethanol, methanol, PEG 400, and dimethyl sulfoxide (DMSO) were purchased from Wako Pure Chemical Industries, Ltd (Osaka, Japan). A 0.45-μm sterilizing filter (EMD Millipore Co., MA, USA), Gibco DMEM/F12, Gibco FBS, Gibco antibiotic solutions (Life Technologies Co., USA), and Dulbecco's modified EAGLE's medium nutrient mixture F-12 HAM (Sigma–Aldrich Co., LLC., St. Louis, MO) were used. A WST-8 cell proliferation assay kit was purchased from Dojindo Molecular Technologies, Inc. (Tokyo, Japan). Laserphyrin® was kindly provided by Meiji Seika Pharma Co., Ltd (Tokyo, Japan). 5-[4-(β-D-Glucopyranosylthio)-2,3,5,6-tetrafluorophenyl]-10,15,20-tris(pentafluorophenyl)porphyrin (H_2Glc**1**),

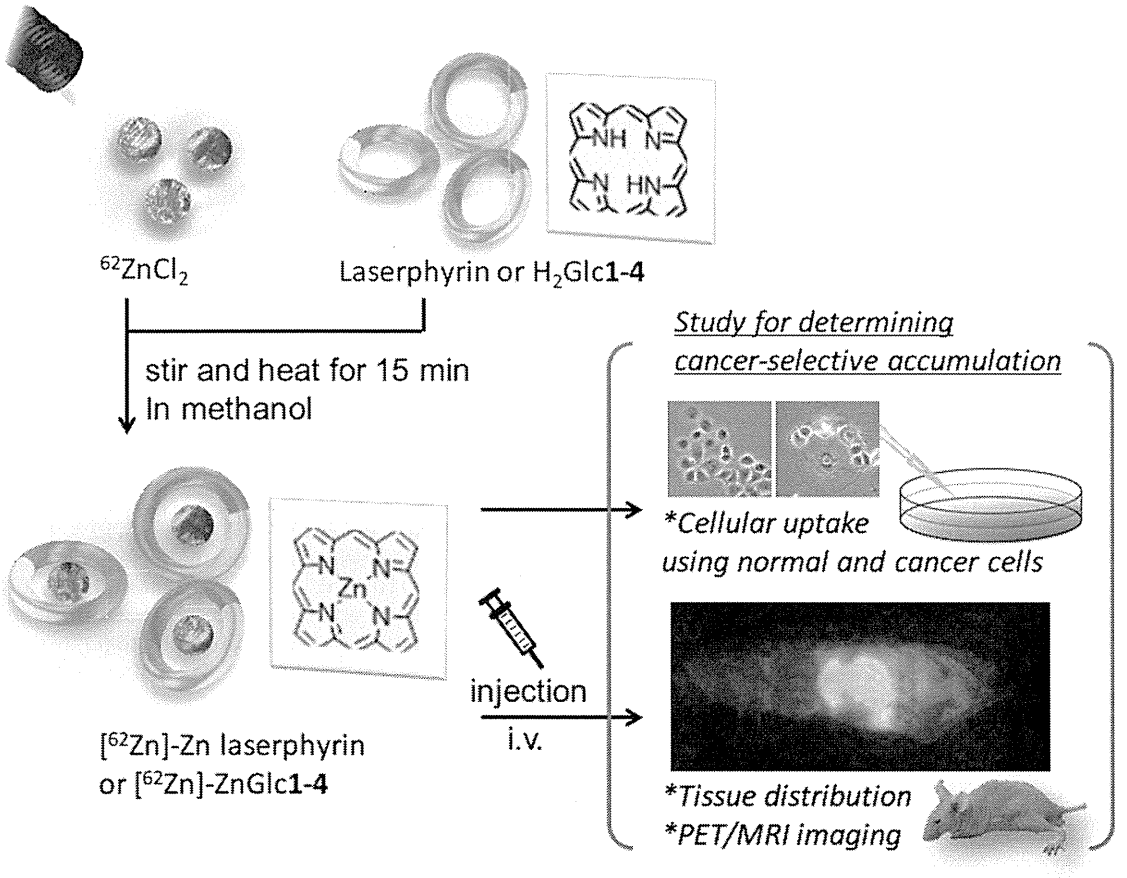

Scheme 1. Schematic diagram of the studies for confirming cancer-selective accumulation by [^{62}Zn]-labeled laserphyrin® and [^{62}Zn]–ZnGlc**1**–**4**.

5,10-bis[4-(β-D-glucopyranosylthio)-2,3,5,6-tetrafluorophenyl]-15,20-bis(pentafluorophenyl)porphyrin (H_2Glc*cis*-**2**), 5,15-bis[4-(β-D-glucopyranosylthio)-2,3,5,6-tetrafluorophenyl]-10,20-bis(pentafluorophenyl)porphyrin (H_2Glc*trans*-**2**), 5,10,15-tris[4-(β-D-glucopyranosylthio)-2,3,5,6-tetrafluorophenyl]-20-pentafluorophenylporphyrin (H_2Glc**3**), 5,10,15,20-tetrakis[4-(β-D-glucopyranosylthio)-2,3,5,6-tetrafluorophenyl]porphyrin (H_2Glc**4**), 5-[4-(β-D-Glucopyranosylthio)-2,3,5,6-tetrafluorophenyl]-10,15,20-tris(pentafluorophenyl)porphyrin zinc complex (ZnGlc**1**), 5,10-bis[4-(β-D-glucopyranosylthio)-2,3,5,6-tetrafluorophenyl]-15,20-bis(pentafluorophenyl)porphyrin zinc complex (ZnGlc*cis*-**2**), 5,15-bis[4-(β-D-glucopyranosylthio)-2,3,5,6-tetrafluorophenyl]-10,20-bis(pentafluorophenyl)porphyrin zinc complex (ZnGlc*trans*-**2**), 5,10,15-tris[4-(β-D-glucopyranosylthio)-2,3,5,6-tetrafluorophenyl]-20-pentafluorophenylporphyrin zinc complex (ZnGlc**3**), and 5,10,15,20-tetrakis[4-(β-D-glucopyranosylthio)-2,3,5,6-tetrafluorophenyl]porphyrin zinc complex (ZnGlc**4**) were prepared according to our previously described methods (Fig. 1, Supporting information Fig. S1).[13,19] Solvents of samples were prepared by mixing 20% vol ethanol, 30% vol PEG 400, and 50% vol distilled water. [^{62}Zn] solution and zinc-65 ([^{65}Zn]) solution were generated by an online preparation system for multitracer solutions at the Research Center for Nuclear Physics (RCNP, Osaka, Japan).[6] Here, we refer to non-radioactive zinc as [Zn].

2.2. Synthesis of [^{62}Zn]- and [^{65}Zn]-bisglycoconjugated porphyrin zinc complexes

[^{65}Zn]-$ZnCl_2$ (5 MBq) or [^{62}Zn]-$ZnCl_2$ (5 MBq) was added to bisglycoconjugated porphyrins, namely H_2Glc*cis*-**2** and H_2Glc*trans*-**2** in methanol (1.5 mM). The reaction mixture was stirred and heated (~60 °C) for about 10 min, until the color changed from brownish-red to pinkish-red, indicating that H_2Glc**1**–**4** had reacted with [^{62}Zn] or [^{65}Zn].

[^{62}Zn]-ZnGlc**1**–**4** was concentrated under reduced pressure, and then 300 μL of [^{62}Zn]-ZnGlc**1**–**4**-solvent was added. These preparations were passed through a 0.45-μm sterilizing filter before use.

2.3. Synthesis of [^{62}Zn]- and [^{65}Zn]-Zn laserphyrin® zinc complex

A procedure similar to that described for [^{62}Zn]- or [^{65}Zn]-glycoconjugated zinc complexes was applied to laserphyrin® to yield [^{62}Zn]- and [^{65}Zn]-Zn laserphyrin®.

2.4. Cell culture

RGM-1 and RGK-1 cells were cultured in DMEM/F12 and DMEM/F-12 HAM, respectively. The culture media contained 10% inactivated fetal bovine serum (FBS) and 1% antibiotic solutions. Both cell lines were cultured in a 5%-CO_2 cell culture incubator at 37 °C.

2.5. Cellular uptake of non-radioactive samples by RGM-1 and RGK-1 cells

Cells were incubated in 6-well dishes at a density of 1×10^6 cells/well for 24 h. Then, 0.5 μM laserphyrin®, H_2Glc*trans*-**2**, [Zn]-Zn laserphyrin®, or [Zn]-ZnGlc**1**–**4** in 1% DMSO/culture medium were exposed to cells for 0–24 h. Samples were extracted from cells by the addition of 100 μL of DMSO after washing with phosphate-buffered saline (PBS) twice. The extracts were centrifuged

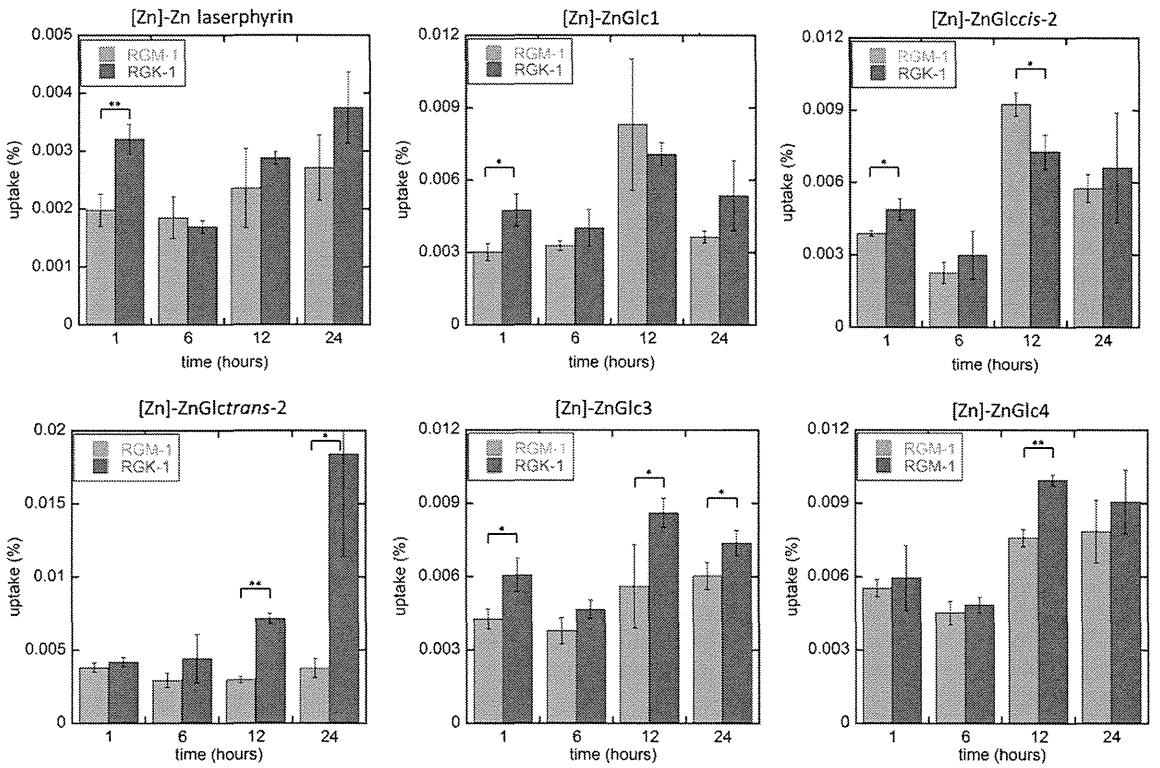

Figure 1. Relative cellular uptake amount of [Zn]-Zn laserphyrin® and [Zn]-ZnGlc**1**–**4** by rat gastric mucosal epithelial cells (RGM-1) and oncogenic RGM-1 mutated cells (RGK-1) cells. RGM-1 and RGK-1 cells (1×10^6 cells/well) were incubated with each chemical (0.5 M) at 37 °C for 1, 6, 12, or 24 h. Cellular uptake was measured by fluorescence intensity. The cellular uptake amount represents the percentage of the total amount of photosensitizer added. The concentration of the photosensitizers was 0.5 M. Values are the mean ± standard deviation of three replicate experiments. Significant differences are denoted as: $^*p$ <0.05, $^{**}p$ <0.01.

for 10 min at 10,000 rpm. Fluorescence intensities of supernatants (50 μL) in 96-well dishes were measured using a plate reader (VarioSkan, Thermo Fisher Scientific K. K., Kanagawa, Japan) at the following wavelengths: Laserphyrin®, Ex. 410 nm and Em. 660 nm; [Zn]-Zn laserphyrin®, Ex. 410 nm and Em. 650 nm; [Zn]-ZnGlc**1**, [Zn]-ZnGlc*cis*-**2**, [Zn]-ZnGlc**3**, Ex. 410 nm and Em. 645 nm; H_2Glc*trans*-**2**, Ex. 400 nm and Em. 701 nm; [Zn]-ZnGlc*trans*-**2**, Ex. 410 nm and Em. 646 nm, and [Zn]-ZnGlc**4**, Ex. 410 nm and Em. 650 nm.

2.6. Cellular uptake of radioactive samples by RGM-1 and RGK-1 cells

Cells were incubated in 6-well dishes at a density of 1×10^6 cells/well for 24 h. Cells were then exposed to 0.5 μM [^{62}Zn]- or [^{65}Zn]-Zn laserphyrin®, ZnGlc*cis*-**2**, and ZnGlc*trans*-**2** for 0–12 h. After being washed with PBS twice, cells were detached with 500 μL of Trypsin/ethylenediaminetetraacetic acid (EDTA) and lysed with 500 μL of 1% Triton X-100. The radioactivity of the extracts was measured by using a γ-counter (TDC-521, Aloka, Tokyo, Japan).

2.7. Tissue distribution in mice with tumors

Five-week-old BALBc/Slc-nu/nu mice were purchased from Japan SLC, Inc. (Shizuoka, Japan). RGK cells (1×10^6 cells/100 μL) were administrated subcutaneously to the outside of the left thigh. The tumor-bearing mice were established 1–2 weeks later. [^{65}Zn]-$ZnCl_2$ or [^{65}Zn]-labeled sample (5×10^4 cpm, 200 μL) was injected through the tail veins. After a prescribed period, the mice were anesthetized with pentobarbital. Blood was then collected via cardiac puncture. The major organs (tumor, brain, heart, lung, liver, kidney, and spleen) were collected and their radioactivity measured using a γ-counter (AccuFlex γ7001, Aloka). The data were normalized to the radioactivity of the injected dose per gram (ID%/g).

2.8. PET/MRI imaging with [^{62}Zn]-labeled samples

PET/MRI imaging was performed as previously described.[20] Briefly, [^{62}Zn]-Zn laserphyrin®, [^{62}Zn]-ZnGlc*cis*-**2**, and [^{62}Zn]-ZnGlc*trans*-**2** (100 μL, 75 μM, 0.5 MBq) were injected into tumor-bearing mice through the tail vein. At 1, 3, and 8 h after the injection, PET/MRI images were captured, with the mice in a prone position and under anesthesia (inhalation of 2% isoflurane through a tube). We performed simultaneous PET/MRI acquisition using iPET/MRI scanner.[21] This scanner has 0.3 T permanent magnet and MRI image was acquired with a fast low angle shot T1-weighted sequence. The following imaging parameters were set; 13.33 MHz NMR frequency, 40 mm field of view (FOV) and 128/256 phase and frequency encodes. The matrix size of MRI image was 256 × 128 with 1.25 mm thickness of slices. PET scanner has 40 mm transaxial FOV and 18.2 mm axial FOV. To cover whole mouse body, five PET acquisitions with different positions were performed. PET data were list-mode data and we first rebinned the list-mode data to two dimentional sinogram data by single slice rebinning technique. The image reconstruction was performed using order subset expectation maximization (OSEM) algorithm with iteration of 3 and subset of 5. No attenuation and scatter corrections were performed due to small size of object.

2.9. Photocytotoxicity of non-radioactive samples into RGM-1 and RGK-1 cells

Cells were incubated for 24 h in 96-well dishes at a density of 5×10^3 cells/well. Cells were then exposed to 2.0 μM [Zn]-laserphyrin® or 1.0 μM [Zn]-ZnGlc*cis*-**2** or 0.5 μM [Zn]-ZnGlc*trans*-**2** for 0–24 h. After cells were washed twice with PBS, fresh culture medium (100 μL) was added. The cells were exposed to light from a 100 W halogen lamp equipped with a water jacket and a Y-50 cut-off filter (λ >500 nm). The light intensity was measured using a UV–vis power meter (ORION/TH, Ophir Optronic Ltd, Jerusalem, Israel). The irradiation time was adjusted to obtain the desired light dose of 16 J cm^{-2}. The mitochondrial NADH dehydrogenase activity of the cells after 24 h of photoirradiation was measured using a WST-8 Cell Proliferation Assay kit according to the manufacturer's instructions. The absorbance at 450 nm was measured using a plate reader. The percentage of cell survival was calculated by normalization, with respect to the absorbance for untreated cells (vehicle).

2.10. Statistical analysis

All statistical evaluations were performed using the Student's *t*-test. All values for cellular uptake were expressed as mean ± standard deviation.

3. Results

3.1. Cancer cell selective uptake of Zn-labeled PET agents

The chemical structures of [Zn]-Zn laserphyrin®, [Zn]-ZnGlc**1**, [Zn]-ZnGlc*cis*-**2**, [Zn]-ZnGlc*trans*-**2**, [Zn]-ZnGlc**3**, and [Zn]-ZnGlc**4** are shown in Chart 1. For determining cancer cell-selective accumulation, normal rat gastric mucosa cells (RGM-1) and cancerous mutant RGM-1 cells (RGK-1) were used.[17] Comparison of the amounts of cellular uptake between normal cells and cancerous cells can easily provide confirmation of cancer selective properties of PET agents in vitro. Figure 1 shows the relative cellular uptake of [Zn]-labeled PET agents, based on autofluorescence. Cellular uptake did not depend on the numbers of modified glucose in glucose-modified PET agents, [Zn]-ZnGlc*trans*-**2**, which showed the maximum amounts of cellular uptake. Although the *cis* isomers had the same numbers of modified glucose as the *trans* isomers, the level of accumulation showed the same tendency as that of other PET agents, except for *trans* isomers. The *trans* isomer also showed cancer cell-selective accumulation, as demonstrated by RGK-1 accumulation of [Zn]-ZnGlc*trans*-**2** being around 4 times more than that of RGM-1 after 24 h. [Zn]-ZnGlc*trans*-**2** appeared to be the best PDT agent in this study, showing properties of cancer cell-selective accumulation.

We also confirmed that Zn-labeling caused a change in cellular uptake (Fig. 2) by seemingly enhancing cancer cell-selective accumulation. Laserphyrin® has greater cellular uptake by Zn-labeling. However, this enhancement was not significant in cancer cell-selective accumulation. Zn-labeled H_2Glc*trans*-**2** clearly showed enhanced cancer cell-selective accumulation after 24 h, with high cellular uptake by 12 h.

Supporting information Figure S2 shows that radioactive zinc-labeled PET reagents, with [^{62}Zn] ion and [^{65}Zn] ion, had the same cellular uptake tendencies as the results with [Zn] ion, shown in Figures 1 and 2.

3.2. Tissue distributions and PET/MRI imaging

Because [Zn]-ZnGlc*trans*-**2** showed high cellular uptake and cancer cell-selective accumulation, we choose [Zn]-ZnGlc*trans*-**2** from [Zn]-ZnGlc**1**–**4** to use in animal experiments. In a tissue distribution study, laserphyrin® and H_2Glc*trans*-**2** labeled with [^{65}Zn] showed half-lives of around 244 days; the half-life of [^{62}Zn] is too short for use in this study. Figure 3 shows the tissue distributions of $^{65}ZnCl_2$, [^{65}Zn]-Zn laserphyrin®, and [^{65}Zn]-ZnGlc*trans*-**2**. [^{65}Zn]-Zn

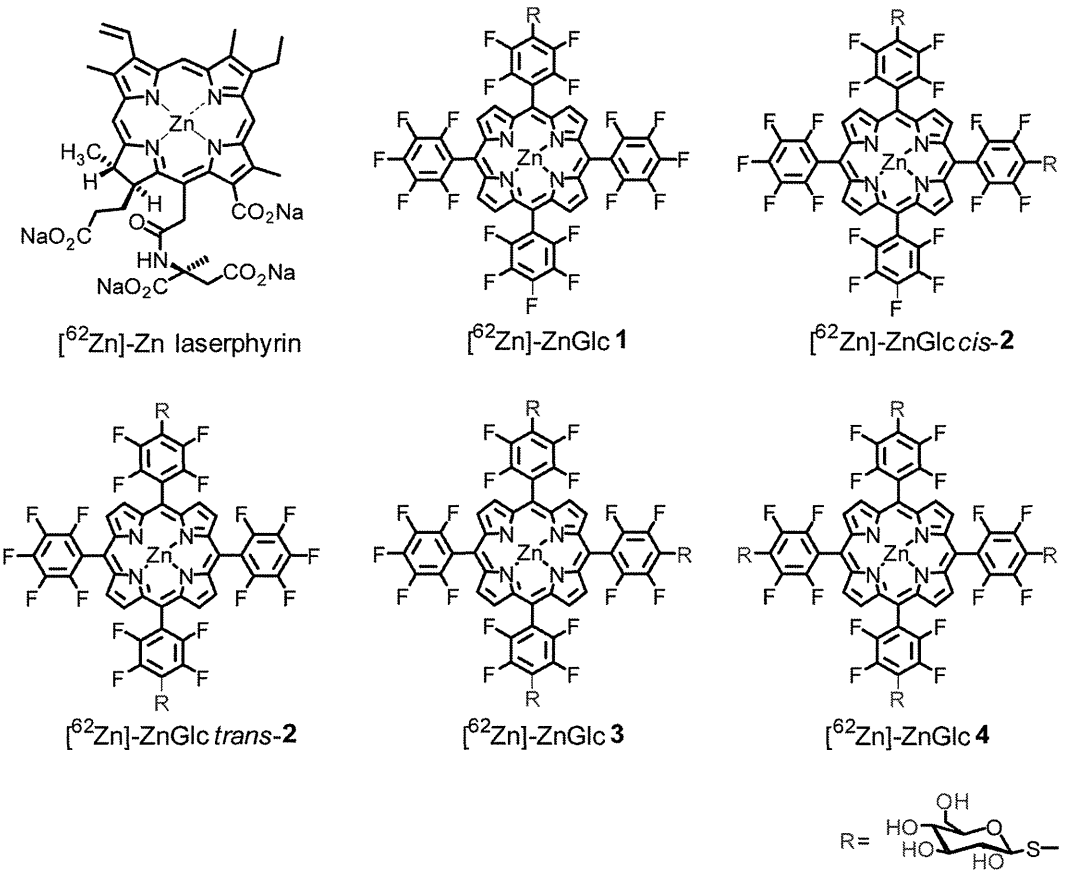

Chart 1. Structures of [^{62}Zn]-Zn laserphyrin® and [^{62}Zn]-ZnGlc**1–4**.

laserphyrin® in the blood decreased in a time-dependent manner, with almost complete elimination within 24 h, while it was still detectable in the liver, kidney, and spleen. Blood levels of $^{65}ZnCl_2$ and [^{65}Zn]-ZnGlc*trans*-**2** did not diminish, and [^{65}Zn]-ZnGlc*trans*-**2** was also detected in the liver, kidney, and spleen, at higher amounts than those of $^{65}ZnCl_2$ and [^{65}Zn]-Zn laserphyrin®.

Detailed tissue distributions were determined. $^{65}ZnCl_2$ and [^{65}Zn]-Zn laserphyrin® diminished from the blood and decreased in tissues over time, whereas [^{65}Zn]-ZnGlc*trans*-**2** remained in the blood and slightly decreased in tissues over time. For PET/MRI imaging with [^{62}Zn]-labeled PET agents, 100 μL of [^{62}Zn]-Zn laserphyrin® and [^{62}Zn]-ZnGlc*trans*-**2** (0.5 MBq) were administered to mice through the tail vein. Figure 4 shows the results of PET/MRI imaging. PET successfully detected [^{62}Zn]-Zn laserphyrin® and [^{62}Zn]-ZnGlc*trans*-**2**, at locations that correspond to our tissue distribution results. Whole body PET/MRI images are shown in Supporting information Movies S1–6.

4. Discussion

Our in vitro study revealed a high level of cellular uptake of [Zn]-ZnGlc*trans*-**2**, with cancer cell-selective accumulation (Fig. 1). This finding was consistent with previous studies of cellular uptake of PET agents without Zn-labeling[13] and those of cancer cells-selective photocytotoxic effects.[14] The substitution numbers were not significant for cellular uptake (Fig. 1). Of note, [Zn]-ZnGlc*trans*-2 accumulated in cancer cells specifically. It indicated that orientations of glycoconjugated porphyrins are more important for cancer cell-selective accumulation than the substitution numbers. Hydrophobicity parameters (Log*P*), which is an index for suggesting an affiliation of cellular membrane, showed in ascending order ZnGlc1 (Log*P* = 5.7), ZnGlc*cis*-2 (Log*P* = 4.8), ZnGlc*trans*-2 (Log*P* = 4.3), ZnGlc3 (Log*P* = 3.4) and ZnGlc4 (Log*P* = 2.2) in previous study.[13] The order of cellular uptake was the same except for [Zn]-ZnGlc*trans*-2 in Figure 1. Therefore, why [Zn]-ZnGlc*trans*-2 showed cancer cell-selective accumulation is difficult to confirm by Log*P*. In this study, cell viability after PDT was decreased an exposure time-dependently (Supporting information Fig. S3), indicating that photocytotoxic effects depend on cellular accumulation. Zn labeling also contributes to cancer-selective accumulation, the extent of which varied from structure to structure (Fig. 2 and Supporting information Fig. S1). Zinc is necessary for the maintenance of homeostasis, playing a role in cellular responses, including cellular uptake.[22,23] Intracellular zinc concentrations in normal cells are regulated and balanced,[24] whereas cancer cells accumulate zinc for proliferation and differentiation.[25,26] Although the expression of zinc transporter in cancer cells is greater than that in normal cells,[23] an exposure of zinc preferentially should enhance endocytosis in cancer cells preferentially. Zinc may be released from Zn-labeled PET agents by metabolism of Zn-labeled samples, and the cellular uptake should be enhanced, especially in cancer cells. Furthermore, porphyrin derivatives also accumulated in cancer cells, specifically through HCP-1.[18,27] The structures of Zn-labeled PET agents used in this study satisfy the requirements of cancer cells and as a result, show cancer cell-selective accumulation.

In our in vivo study, cancer-specific accumulation was consistent with the results of cellular uptake, with [^{65}Zn]-ZnGlc*trans*-**2** more detectable in tumors than [^{65}Zn]-Zn laserphyrin® (Fig. 3). The major difference in tissue distributions was related to the blood circulation time, which probably caused the difference in accumulation in the tumor. The actual shapes of the compounds

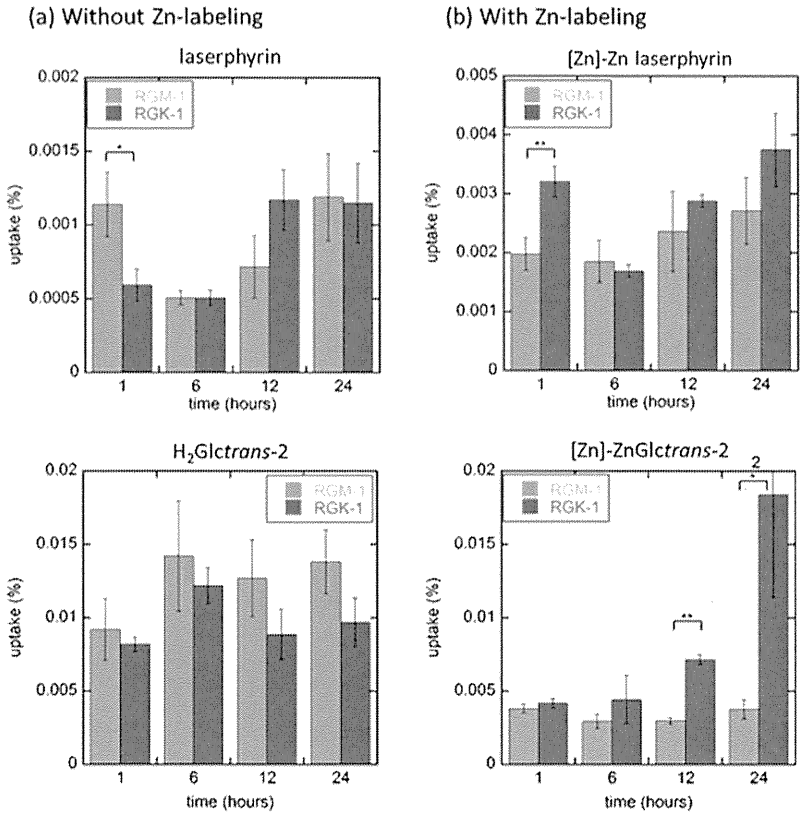

Figure 2. Relative cellular uptake amount by rat gastric mucosal epithelial cells (RGM-1) and oncogenic RGM-1 mutated cells (RGK-1) cells of laserphyrin® and H_2Glc*trans*-**2** with or without Zn-labeling. RGM-1 and RGK-1 cells (1×10^6 cells/well) were incubated with of each chemical (0.5 M) at 37 °C for 1, 6, 12, or 24 h. Cellular uptake was measured by fluorescence intensity. The cellular uptake amount represents the percentage of the total amount of photosensitizer added. Values are the mean ± standard deviation of three replicate experiments. Significant differences were denoted as: $^*p$ <0.05, $^{**}p$ <0.01.

in the blood were not determined. However, the results suggest 2 possibilities of the structure in the blood: the biologically inactive form or a formulation of complexes, in conjunction with blood components, such as albumin. For example, biologically inactive nanocarriers[28] and blood components[29] show long blood-circulation periods. Nanocarriers were designed, by modifying polyethylene glycol[30] and maintaining the proper size for blood circulation,[31] to avoid rapid clearance by the immune system, and as a result, nanocarriers are mainly detected in the blood and blood-rich tissues, such as the liver, spleen, and kidney.[28] These nanocarriers also have enhanced permeability and retention (EPR) effects,[32] without interacting with blood components. On the other hand, some blood components permit chemicals to circulate in the blood for a long time by forming complexes.[33] For example, albumin, with a plasma half-life of 3–4 days in vivo, forms complexes of cationic chemicals, and the complexes show long blood circulation periods. The ζ potential of the albumin-modified complex decreased in a concentration-dependent manner.[34] A ζ potential between neutral and negative is adequate for blood circulation,[30] which is one of the reasons that an albumin complex enhances blood circulation. Modifications of other blood components also enhance the hemocompatibility of chemicals.[33] [^{65}Zn]-ZnGlc*trans*-**2** likely circulates in the blood after forming complexes with blood components because the tissue distributions are close to the results observed with [^{65}Zn]-$ZnCl_2$, which mainly forms complexes with albumin in the blood.[35] This may contribute to tissue distribution.

Although PET/MRI imaging takes 25 min per one whole body image, PET/MRI images may include the change of tissue distribution. According to Figure 3, the tendency of tissue distribution from 1 to 3 h was not significant. Therefore we suggested that PET/MRI images should not be changed significantly within the duration time. However, we are difficult to discuss about the detail of pharmacokinetics from only PET/MRI images.

Long blood circulation time is favorable for cancer-selective accumulation; this was especially true for [^{65}Zn]-ZnGlc*trans*-**2** in this study, which obscured the cancer in the PET image (Fig. 4). In order to visualize the cancer clearly, a difference in signal contrast between the tumor and surrounding tissues is required. In fact, the accumulation in cancer at left leg is difficult to see in PET/MRI images (Fig. 4) because an accumulation in liver was too high compared to in tumor (Fig. 3). For resolving this problem, we have been determining the conjugate points between chemical properties and biological reactions to create a further multi-functional PET agent.

ZnGlc**1**–**4** should be applied as an antioxidant, and not only a PET agent, for inhibiting the side effects of PDT through suppression of inflammation. Zinc is a basic component of antioxidants in the blood,[36] and zinc porphyrin is well known as a scavenger of reactive oxygen species (ROS).[37] ROS scavengers are expected to suppress cancerous growth, invasion, and metastasis[17,38,39] and inhibit inflammation in the intestine.[40] We showed cancer-selective PDT effects in Supporting information Figure S3 and in a previous report,[14] which suggest that ZnGlc**1**–**4** may be become an ideal therapeutic and diagnostic agent in PDT and PET, respectively.

5. Conclusions

[^{62}Zn]-ZnGlc*trans*-**2** showed cancer-selective accumulation, and the amount of cellular uptake in cancerous gastric cells was around 4-times more than that in normal gastric cells. The cellular uptake

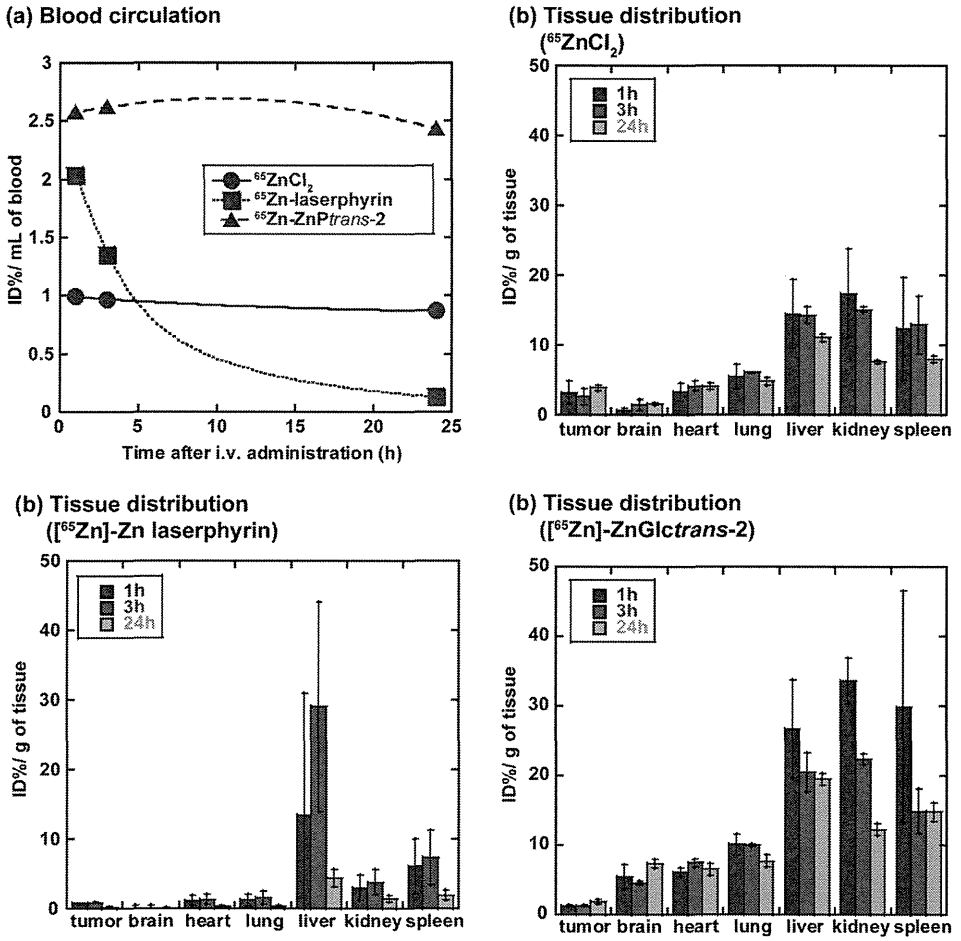

Figure 3. Tissue distribution after administration through the tail vein of $^{65}ZnCl_2$, [^{65}Zn]–Zn laserphyrin®, or [^{65}Zn]-ZnGlc*trans*-**2** in oncogenic rat gastric mucosal epithelial mutated cells (RGK-1) tumor model mice. 200 μL of $^{65}ZnCl_2$, [^{65}Zn]–Zn laserphyrin®, or [^{65}Zn]–ZnGlc*trans*-**2** (5×10^4 cpm) was injected. The mice were anesthetized, tissues were dissected, and radioactivity of [^{65}Zn] from dissected tissues was detected by using a γ counter. (a) Injected dose (ID) % of 1 mL of blood. (b) ID% of 1 g of tissue (tumor, brain, heart, lung, liver, kidney, and spleen). Values are the mean ± standard deviation of three replicate experiments.

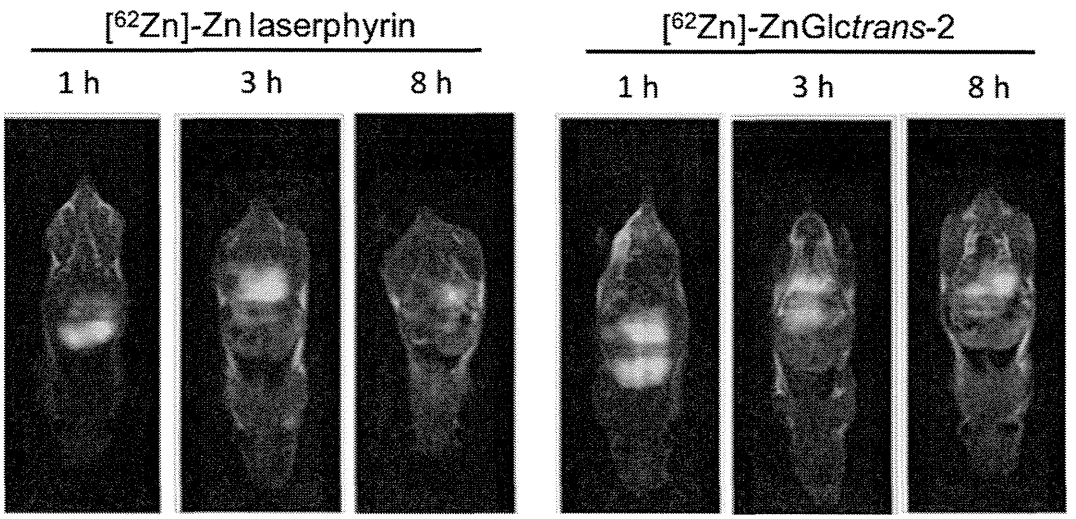

Figure 4. PET/MRI imaging of [^{62}Zn]–Zn laserphyrin® and [^{62}Zn]–ZnGlc*trans*-**2**. These images were acquired after intravenous administration of [^{62}Zn]–Zn laserphyrin® and [^{62}Zn]–ZnGlc*trans*-**2** (0.5 MBq, 100 μL, 75 μM) through the tail vein. Whole body PET/MRI images are shown in Supporting Information Movie S1–6.

by cancer cells nearly coincides with the results of cancer accumulation in vivo. [^{62}Zn]-ZnGlc*trans*-**2** circulated in the blood for over 24 h without decreasing and showed greater accumulation in cancer compared to other PET agents used in this study.

Acknowledgements

Laserphyrin® (Laserphyrin) was kindly provided by Meiji Seika Pharma Co., Ltd (Tokyo, Japan). This study was partially supported

by JSPS KAKENHI Grant number 24229008 and 236599576, the NAIST Presidential Special Fund, Japan Science and Technology Agency (JST), the A-Step Feasibility Study Program (AS242Z01752P), Grants from the Terumo Life Science Foundation, and a Grant for molecular imaging from the Japan Science Technology Agency. The authors thank Mr. Yumiko Ito, Shinji Fujiyama, Kasumi Fujitake, Taishi Tomiyama (Department of Chemical and Biological Engineering, Ube National Collage of Technology), and Dr. Hiroki Tanimoto (NAIST) for helpful discussion and kind support.

Supplementary data

Supplementary data associated with this article can be found, in the online version, at http://dx.doi.org/10.1016/j.bmc.2014.02.021.

References and notes

1. Waki, A.; Fujibayashi, Y.; Yokoyama, A. *Nucl. Med. Biol.* **1998**, *25*, 589.
2. Kim, D.-Y.; Kim, H.; Yu, K.; Min, J. *Bioconjug. Chem.* **2012**, *23*, 431.
3. Fischer, C. R.; Müller, C.; Reber, J.; Müller, A.; Krämer, S. D.; Ametamey, S. M.; Schibli, R. *Bioconjug. Chem.* **2012**, *23*, 805.
4. Guerrero, S.; Herance, J. R.; Rojas, S.; Mena, J. F.; Gispert, J. D.; Acosta, G. A.; Albericio, F.; Kogan, M. J. *Bioconjug. Chem.* **2012**, *23*, 399.
5. Mu, L.; Honer, M.; Becaud, J.; Martic, M.; Schubiger, P. A.; Ametamey, S. M.; Stellfeld, T.; Graham, K.; Borkowski, S.; Lehmann, L.; Dinkelborg, L.; Srinivasan, A. *Bioconjug. Chem.* **2010**, *21*, 1864.
6. Kasamatsu, Y.; Yatsukawa, M.; Sato, W.; Ninomiya, K.; Ohki, T.; Takahashi, N.; Yokoyama, A.; Kikunaga, H.; Kinoshita, N.; Shibata, S.; Shinohara, A. *Appl. Radiat. Isot.* **2008**, *66*, 271.
7. Ting, R.; Aguilera, T. A.; Crisp, J. L.; Hall, D. J.; Eckelman, W. C.; Vera, D. R.; Tsien, R. Y. *Bioconjug. Chem.* **2010**, *21*, 1811.
8. Liu, S. *Bioconjug. Chem.* **2009**, *20*, 2199.
9. Bernstein, E. J.; Schmidt-Lauber, C.; Kay, J. *Best Pract. Res. Clin. Rheumatol.* **2012**, *26*, 489.
10. Yeung, E. W.; Allen, D. G. *Clin. Exp. Pharmacol. Physiol.* **2004**, *31*, 551.
11. Haynes, N. G.; Lacy, J. L.; Nayak, N.; Martin, C. S.; Dai, D.; Mathias, C. J.; Green, M. A. *J. Nucl. Med.* **2000**, *41*, 309.
12. Welch, M. J.; McCarthy, T. J. *J. Nucl. Med.* **2000**, *41*, 315.
13. (1) Hirohara, S.; Nishida, M.; Sharyo, K.; Obata, M.; Ando, T.; Tanihara, M. *Bioorg. Med. Chem.* **2010**, *18*, 1526; (2) Hirohara, S.; Sharyo, K.; Kawasaki, K.; Totani, M.; Tomotsuka, A.; Funasako, R.; Yasui, N.; Hasegawa, Y.; Yuasa, J.; Nakashima, T.; Kawai, T.; Oka, C.; Kawaichi, M.; Obata, M.; Tanihara, M. *Bull. Chem. Soc. Jpn.* **2013**, *86*, 1295.
14. Tamura, M.; Matsui, H.; Hirohara, S.; Kakiuchi, K.; Tanihara, M.; Takahashi, N.; Nakai, K.; Kanai, Y.; Watabe, H.; Hatazawa, J. *Chem. Lett.* in press, http://dx.doi.org/10.1246/cl.140056.
15. Kobayashi, I.; Kawano, S.; Tsuji, S.; Matsui, H.; Nakama, A.; Sawaoka, H.; Masuda, E.; Takei, Y.; Nagano, K.; Fusamoto, H.; Ohno, T.; Fukutomi, H.; Kamada, T. *In Vitro Cell. Dev. Biol. Anim.* **1996**, *32*, 259.
16. Shimokawa, O.; Matsui, H.; Nagano, Y.; Kaneko, T.; Shibahara, T.; Nakahara, A.; Hyodo, I.; Yanaka, A.; Majima, H. J.; Nakamura, Y.; Matsuzaki, Y. *In Vitro Cell. Dev. Biol. Anim.* **2008**, *44*, 26.
17. Tamura, M.; Matsui, H.; Tomita, T.; Sadakata, H.; Indo, H. P.; Majima, H. J.; Kaneko, T.; Hyodo, I. *J. Clin. Biochem. Nutr.* **2013**, *54*(1), 12–17.
18. Hiyama, K.; Matsui, H.; Tamura, M.; Shimokawa, O.; Hiyama, M.; Kaneko, T.; Nagano, Y.; Hyodo, I.; Tanaka, J.; Miwa, Y.; Ogawa, T.; Nakanishi, T.; Tamai, I. *J. Porphyrins Phthalocyanines* **2012**, 1.
19. Hirohara, S.; Obata, M.; Alitomo, H.; Sharyo, K.; Ando, T.; Yano, S.; Tanihara, M. *Bioconjug. Chem.* **2009**, *20*, 944.
20. Tatsumi, M.; Yamamoto, S.; Imaizumi, M.; Watabe, T.; Kanai, Y.; Aoki, M.; Kato, H.; Shimosegawa, E.; Hatazawa, J. *Ann. Nucl. Med.* **2012**, 444.
21. Yamamoto, S.; Watabe, H.; Kanai, Y.; Watabe, T.; Aoki, M.; Sugiyama, E.; Kato, K.; Hatazawa, J. *Med. Phys.* **2012**, *39*, 6660.
22. Fukada, T.; Yamasaki, S.; Nishida, K.; Murakami, M.; Hirano, T. *J. Biol. Inorg. Chem.* **2011**, *16*, 1123.
23. Murakami, M.; Hirano, T. *Cancer Sci.* **2008**, *99*, 1515.
24. Eide, D. J. *Biochim. Biophys. Acta* **2006**, *1763*, 711.
25. Hogstrand, C.; Kille, P.; Nicholson, R. I.; Taylor, K. M. *Trends Mol. Med.* **2009**, *15*, 101.
26. Franklin, R. B.; Costello, L. C. *Arch. Biochem. Biophys.* **2007**, *463*, 211.
27. Diamond, I.; Granelli, S. G.; McDonagh, A. F.; Nielsen, S.; Wilson, C. B.; Jaenicke, R. *Lancet* **1972**, *2*, 1175.
28. Mosqueira, V. C.; Legrand, P.; Morgat, J. L.; Vert, M.; Mysiakine, E.; Gref, R.; Devissaguet, J. P.; Barratt, G. *Pharmacol. Res.* **2001**, *18*, 1411.
29. Pavlovskis, O. R.; Shackelford, A. H. *Infect. Immun.* **1974**, *9*, 540.
30. Tamura, M.; Ichinohe, S.; Tamura, A.; Ikeda, Y.; Nagasaki, Y. *Acta Biomater.* **2011**, *7*, 3354.
31. Alexis, F.; Pridgen, E.; Molnar, L. K.; Farokhzad, O. C. *Mol. Pharm.* **2008**, *5*, 505.
32. Maeda, H.; Wu, J.; Sawa, T.; Matsumura, Y.; Hori, K. *J. Controlled Release* **2000**, *65*, 271.
33. Maeda, H.; Seymour, L. W.; Miyamoto, Y. *Bioconjug. Chem.* **1992**, *3*, 351.
34. Oupický, D.; Konák, C.; Dash, P. R.; Seymour, L. W.; Ulbrich, K. *Bioconjug. Chem.* **1999**, *10*, 764.
35. Giroux, E. L.; Henkin, R. I. *Biochim. Biophys. Acta* **1972**, *273*, 64.
36. Hughes, S.; Samman, S. *J. Am. Coll. Nutr.* **2006**, *25*, 285.
37. Kashiwagi, Y.; Imahori, H.; Araki, Y.; Ito, O.; Yamada, K.; Sakata, Y.; Fukuzumi, S. *J. Phys. Chem. A* **2003**, *107*, 5515.
38. Kattan, Z.; Minig, V.; Leroy, P.; Dauça, M.; Becuwe, P. *Breast Cancer Res. Treat.* **2008**, *108*, 203.
39. Weaver, A. M. *Sci. Signal.* **2009**, *2*, pe56.
40. Vong, L. B.; Tomita, T.; Yoshitomi, T.; Matsui, H.; Nagasaki, Y. *Gastroenterology* **2012**, *143*, 1027. e3.

Ann Nucl Med (2014) 28:232–240
DOI 10.1007/s12149-013-0800-y

ORIGINAL ARTICLE

Development of a high-resolution YSO gamma camera system that employs 0.8-mm pixels

Seiichi Yamamoto · Hiroshi Watabe · Yasukazu Kanai · Katsuhiko Kato · Jun Hatazawa

Received: 13 September 2013 / Accepted: 14 December 2013 / Published online: 18 January 2014

Abstract
Objective YSO (Ce-doped Y_2SiO_5) is a promising scintillator for a single-photon imaging system since it has relatively high light output and does not contain any natural radioactivity. Since YSO is not hygroscopic, it may be possible to fabricate a block with small pixels for a high-resolution system. For this purpose, we developed a high-resolution gamma camera system that employs smaller than 1-mm YSO pixels.
Methods The gamma camera's detector used 0.8 × 0.8 × 7-mm YSO pixels. All the surfaces of these YSO pixels were mechanically polished, combined with a 0.1-mm-thick $BaSO_4$ reflector to form a 48 × 48 matrix, and optically coupled to a high quantum efficiency, 2-inch square position sensitive photomultiplier tube (Hamamatsu Photonics H10966 A-100). The YSO block was 43.2 × 43.2 mm. The YSO gamma camera was encased in a 5-mm-thick tungsten container, and a parallel collimator was mounted on its front. The parallel hole collimator was made of a 3-layer (each layer was 5-mm thick) tungsten plate, and each plate had 48 × 48, 0.6-mm holes that were positioned by one-to-one coupling with the YSO pixels.
Results Even with the 0.8-mm YSO pixels, we clearly resolved most of the pixels in a 2-dimensional histogram with a peak-to-valley ratio of 2.9 for the 122-keV gamma photons. The energy resolution was 20.4 % FWHM. The spatial resolutions with a parallel hole collimator 2 mm from the collimator surface were 0.7- and 1.3-mm FWHM for the 122- and ~35-keV gamma photons, respectively. We successfully obtained phantoms and small animal images with our YSO gamma camera system.
Conclusion Our high-resolution system has a potential to be useful for molecular imaging research.

Keywords YSO · HQE PSPMT · Gamma camera · High resolution · Tungsten collimator

S. Yamamoto (✉) · K. Kato
Department of Radiological and Medical Laboratory Sciences, Nagoya University Graduate School of Medicine, 1-1-20 Daiko-Minami, Higashi-ku, Nagoya 461-8673, Japan
e-mail: s-yama@met.nagoya-u.ac.jp

H. Watabe · Y. Kanai · J. Hatazawa
Department of Molecular Imaging, Osaka University Graduate School of Medicine, Suita, Japan

Present Address:
H. Watabe
CYRIC, Tohoku University, Sendai, Japan

J. Hatazawa
Department of Nuclear Medicine and Tracer Kinetics, Osaka University Graduate School of Medicine, Suita, Japan

Introduction

There has been considerable work done in developing high-resolution single-photon emission tomography (SPECT) systems for small animals over the last 10 years [1–3]. Most of the recent systems used large field-of-view (FOV) NaI(Tl)-based gamma cameras combined with pinhole collimators to achieve high resolution using the magnification of the pinhole. To reduce the size of the SPECT systems, high-resolution position-sensitive gamma detectors are needed. To achieve high-resolution SPECT based on gamma cameras, a scintillator with high light output is essential to achieve high resolution [4]. Table 1 compares the primary scintillators used for medical imaging systems. YSO (Ce doped Y_2SiO_5) is a promising scintillator for single-photon imaging systems, since it has

Table 1 Comparison of scintillator performances (Hitachi Chemical Co. home page: http://www.hitachi-chem.co.jp/english/products/cc/017.html)

	GSO	BGO	LSO	YSO	NaI:Tl
Density (g/cm^3)	6.71	7.13	7.4	4.45	3.67
Decay time (ns)	30–60	300	40	40	230
Light yield	20	7–12	40–75	30–45	100
Internal radiation?	No	No	Yes	No	No
Hygroscopic?	No	No	No	No	Strong

relatively high light output and does not contain any natural radioactivity. NaI(Tl) has high light output and is widely used for single-photon detection systems such as scintillation cameras [5, 6]. However, its high hygroscopic characteristic prevents the fabrication of scintillator blocks with small pixels and greatly increases the fabricating cost. Since YSO is not hygroscopic, it may be possible to fabricate a block with pixels smaller than 1 mm to realize a high-resolution single-photon imaging system. YSO was previously used as a detector for a hybrid PET/SPECT system that combined LSO and YSO in a dual layer configuration [7]. However, after that trial, it was not used for a single-photon imaging system.

Recently, PSPMTs with high quantum efficiency (HQE) have been developed. By combining these PSPMTs with pixelated YSOs, we can improve the performance of gamma cameras for low-energy gamma photons because an HQE PSPMT is more effective for smaller light signals [8]. To realize a high-resolution single-photon imaging system, we developed a gamma camera that employs smaller than 1-mm YSO pixels. Compared with another approach that achieves high spatial resolution imaging for single-photon emitting radionuclide, such as semiconductor detectors CdTl or CZT [9–11], scintillator-based gamma camera systems have advantages of relatively low cost because semiconductor-based detectors require application-specific integrated circuits (ASIC), whose development cost is very high for front-end electronics in addition to the cost of the detector materials themselves.

Another challenge for this YSO gamma camera is developing a one-to-one tungsten parallel hole collimator that matches the YSO whose pixels are <1 mm. By expanding the technology on manufacturing stacked thin collimators [12], we realized a high-resolution matched collimator that can select the optimum combination of sensitivity and spatial resolution by changing the number for this YSO high-resolution gamma camera.

We previously developed a GSO gamma camera with a similar concept [12]. Because the GSO gamma camera was useful for the whole body imaging of small animals with high sensitivity performance, it was routinely used for molecular imaging research. However, its spatial resolution was not sufficient for measurements in which high resolution was required because the pixel size of the GSO was 1.9 × 1.9 mm, which is relatively large. High-resolution gamma camera will be a powerful instrument for imaging small structures of mouse or rat. Also, high-resolution gamma camera is a key component for the development of high-resolution SPECT systems. In this work, to realize high resolution, we dramatically decreased the size of the YSO pixels to <1 mm, which is less than half of the previous system, and measured the performance.

Materials and methods

Detector

The gamma camera's detector used 0.8 × 0.8 × 7-mm YSO pixels. All the surfaces of these YSO pixels were mechanically polished. They were combined with a 0.1-mm-thick $BaSO_4$ reflector to form a 48 × 48 matrix. The 43.2 × 43.2-mm YSO block was optically coupled to a HQE 2-inch square position sensitive photomultiplier tube (PSPMT: Hamamatsu Photonics H10966 A-100). The quantum efficiency of HQE PSPMT at peak emission wavelength of YSO (420 nm) is 33 %, 1.4 times higher than normal quantum efficiency (NQE) PSPMT [8]. Using an HQE PSPMT improves the position and energy performance.

Collimator

The YSO gamma camera was encased in a 5-mm-thick tungsten container and a parallel collimator was mounted on its front. Figure 1a shows the parallel hole collimators. The parallel collimator was made of a 3-layer (each layer is 5-mm thick) tungsten plate, and each had 48 × 48, 0.6-mm round holes (Fig. 1b) positioned at a one-to-one coupling with the YSO pixels.

Figure 1c shows the entire view of the detector part of the YSO gamma camera system. We can select a desirable combination of sensitivity and spatial resolution by selecting the proper number of layers of the parallel hole collimators [12]. The detector part weighed approximately 2.6 kg.

Data acquisition system

The signals from the PSPMT anodes are read by 64 small-diameter coaxial cables and fed to the gain-control amplifiers that tune the gain variations of the PSPMT anodes. The gain variation adjustments were conducted using the anode gain data provided by Hamamatsu Photonics to compensate for the gain variations. The outputs of the gain-controlled amplifiers are fed to the weight-summing amplifiers, whose calculation was performed using operational amplifiers to

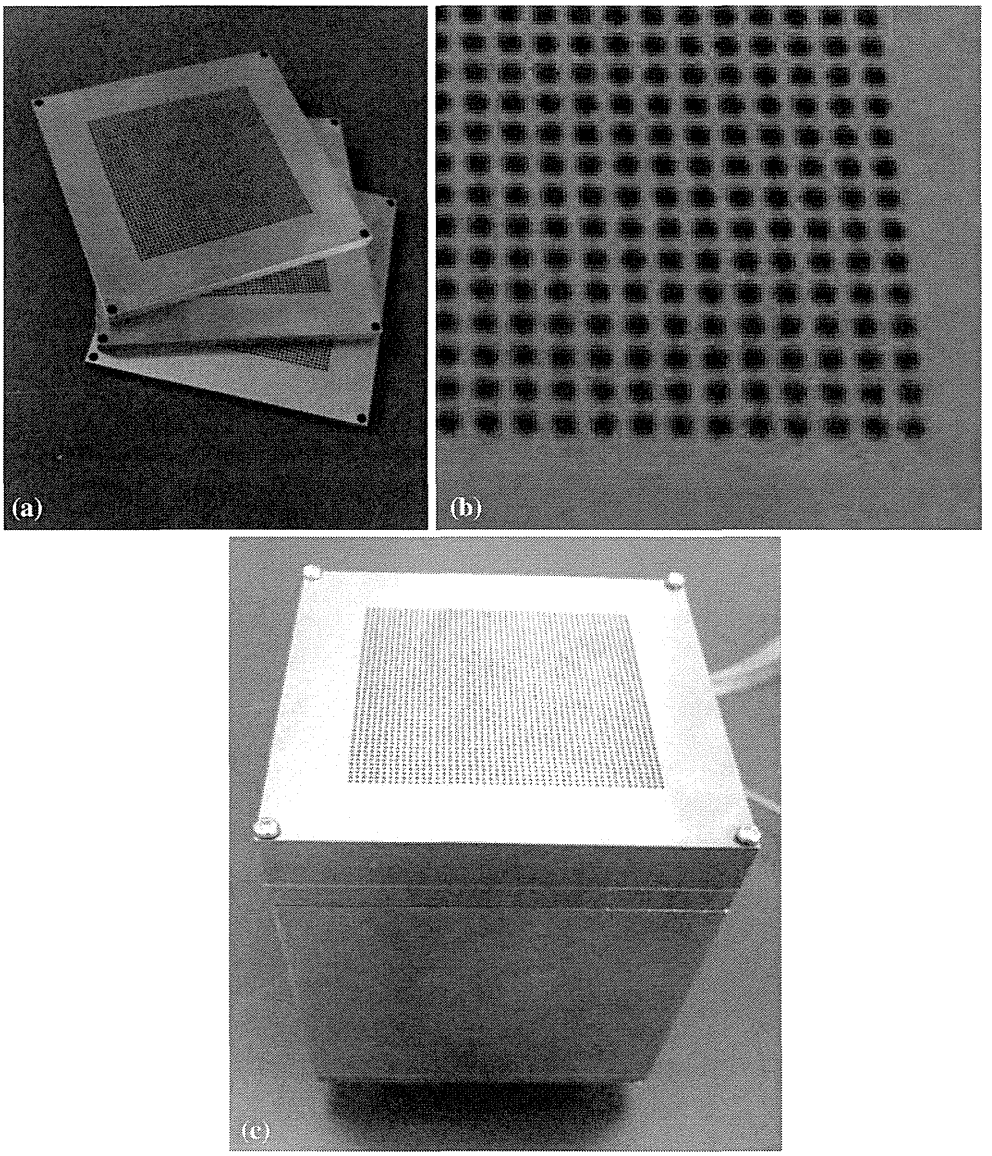

Fig. 1 Tungsten-based parallel hole collimators (**a**), magnified collimator photo (**b**), and whole view of detector part of YSO gamma camera (**c**)

produce two weight-summed signals each for two opposite X directions ($X+$ and $X-$) and Y directions ($Y+$, and $Y-$). These four analog signals are digitized by 100-MHz free running A-D converters and fed to the data acquisition system based on a field programmable gate array (FPGA). The digitally calculated positions ($X+/(X++X-)$ and $Y+/(Y++Y-)$) and energy ($X++X-$) in the FPGA are accumulated in the memory and transferred to a PC. The data acquisition system is basically the same as that used in gamma camera systems [13, 14].

Performance evaluation

For the performance evaluation of the gamma camera system, we measured the light output of YSO, the 2-dimensional position histogram, the energy resolution, the phantom images, and the system spatial resolution and its sensitivity. We also conducted small animal studies. We set energy window of ±20 % for the phantom images, the system spatial resolution, the sensitivity and the small animal studies.

Light output of YSO

First, we measured the energy spectrum for YSO and compared with some of the other scintillators, GSO and LGSO to confirm that the light output of YSO was larger. One of these scintillators was set on a 3-inch round photomultiplier tube (PMT) (R6233-100: Hamamatsu

Photonics, Japan) and covered with a reflector (3 M, ESR). Signals from PMT were fed to a standard NIM module and multichannel analyzer (MCA) (ADC Model 1125P, Clear-Pulse Co., Tokyo) to measure the energy spectra. A Co-57 (122 keV) point source (1-mm diameter, 9 kBq) was used and acquired for 600 s.

Two-dimensional position histogram

We acquired a 2-dimensional position histogram using a Co-57 (122 keV) point source (1-mm diameter, 9 kBq) positioned ~8 cm above the detector surface of the GSO gamma camera. The data were acquired without collimators for 10 h. The peak-to-valley ratios along the profiles in the horizontal and vertical directions were measured and calculated.

Energy resolution

The energy spectrum was measured by setting a region of interest (ROI) for one of the YSO pixels of the 2-dimensional histogram measured for Co-57 gamma photons.

Phantom images

For evaluating the image quality, we measured the following phantom images: the uniformity, the bar phantom for the spatial resolution evaluation and the square slit for the spatial linearity demonstration. In the bar phantom, the slit widths were 2.5, 2, 1.5 and 1 mm (Fig. 2a). In the linearity phantom, we used 2-mm slit widths and 8-mm separations (Fig. 2b). These phantoms were made of 5-mm-thick tungsten. The images were measured using a

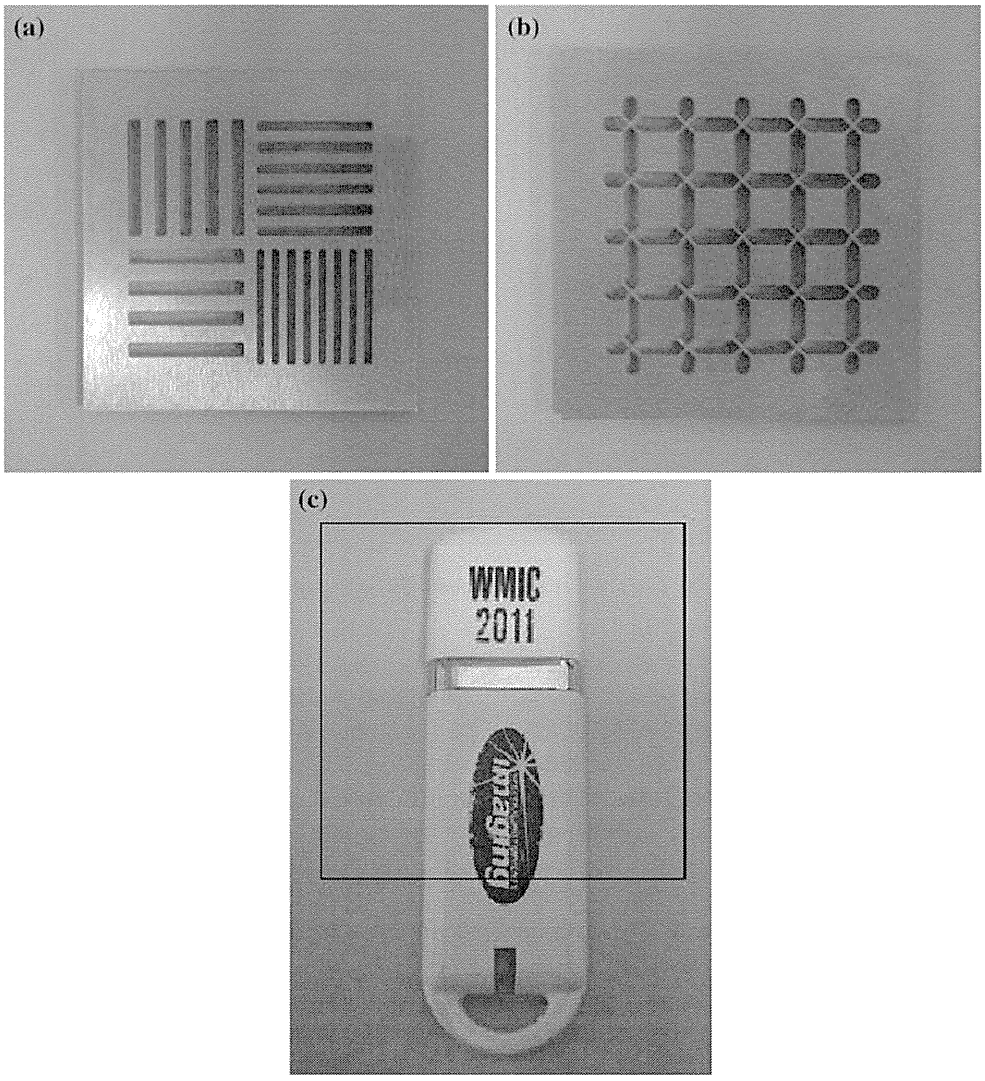

Fig. 2 Phantoms used for image quality demonstration: bar phantom (**a**), square phantom (**b**), and USB memory for transmission images (**c**). The *square mark* in **c** indicates the area measured in transmission image

Co-57 (122 keV) point source (1-mm diameter, 9 kBq) positioned ~8 cm above the detector surface of the gamma camera for 3600 s. These phantoms were positioned on the detector surface, except for the uniformity data acquisition. The slit phantom image was also acquired using I-125 (~35 keV) gamma photons from 1-mm-diameter point source (~100 kBq) for 600 s. Uniformity was estimated by calculating the difference of the maximum pixel value and minimum pixel value and dividing by the mean pixel value in the image.

We also measured the transmission images of a USB memory stick (Fig. 2c) to demonstrate the camera's high resolution. The USB memory stick was positioned between the gamma camera and an I-125 point source (1-mm diameter, ~100 kBq), and USB transmission images were acquired with different magnification ratios. All of these data were acquired without collimators for 600 s.

System spatial resolution

We measured the system spatial resolution with parallel hole collimators mounted in front of the detector surface for one to three layers (5- to 15-mm thick) as a function of the distance from the collimator surface. The measurements were conducted using Co-57 (1-mm diameter, 9 kBq) and I-125 (1-mm diameter, ~100 kBq) point sources for 600 s at each position.

System sensitivity with collimators

We measured the system sensitivity using a Co-57 point source (1-mm diameter, 9 kBq). The Co-57 source was positioned at the center of the FOV of the GSO gamma camera with collimators to obtain the count rate for 600 s. The sensitivity measurements were made for one to three layers (5- to 15-mm thick) as a function of the distance from the collimator surface.

Small animal imaging

To demonstrate the usefulness of our developed gamma camera, rat images were measured. We intravenously administered approximately ~150 MBq (~4 mCi) of Tc-99 m methylene diphosphonate (MDP) into a normal Wistar rat from the tail vein under anesthesia (Pentobarbital, Fujifilm RI Pharma, Japan). The study was performed under the guidelines of the Laboratory Investigation Committee of the Osaka University Graduate School of Medicine. Collimators with two, 10-mm-thick layers were attached to the gamma camera. Imaging started approximately 1.5 h after injection. The rat was imaged at five axial positions with 40-mm intervals. The acquisition time at each point was 5 min. We carefully kept the distance from the collimator surface to the rat as small as possible, less than 1 mm at the minimum point, to improve the resolution.

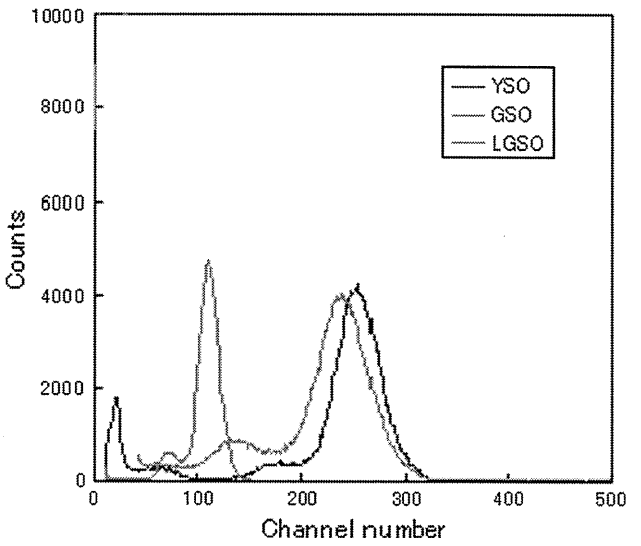

Fig. 3 Energy spectra for YSO, GSO, and LGSO

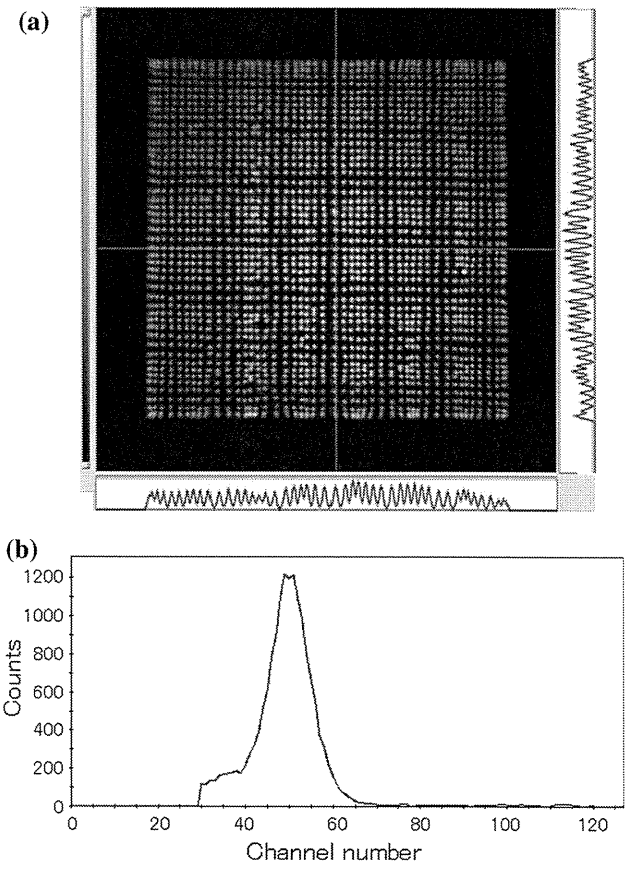

Fig. 4 Two-dimensional histogram of YSO gamma camera for 122-keV gamma photons (**a**) and energy spectrum (**b**)

Results

Light output of YSO

Figure 3 shows the energy spectra for YSO, GSO, and LGSO. YSO's light output resembles that of LGSO, whose light output resembles that of LSO and was ~2.5 times higher than GSO.

Two-dimensional position histogram

The two-dimensional histogram of the YSO gamma camera for 122-keV gamma photons is shown in Fig. 4a. Even with 0.8-mm YSO pixels, we clearly resolved most of the pixels in it with a peak-to-valley ratio of 2.9.

Energy resolution

We show an energy spectrum for one pixel of the YSO scintillators in the two-dimensional histogram in Fig. 4b. The energy resolution was 20.4 % FWHM.

Phantom images

We show the uniformity images of the YSO gamma camera system in Fig. 5a. The uniformity was ±14 %. We also show slit phantom images measured with Co-57 (122 keV) and I-125 (~35 keV) in Fig. 5b and c, respectively. 1-mm slits can be resolved for both 122- and 36-keV gamma photons. However, the separation was better for the 122-keV gamma photons. The linearity

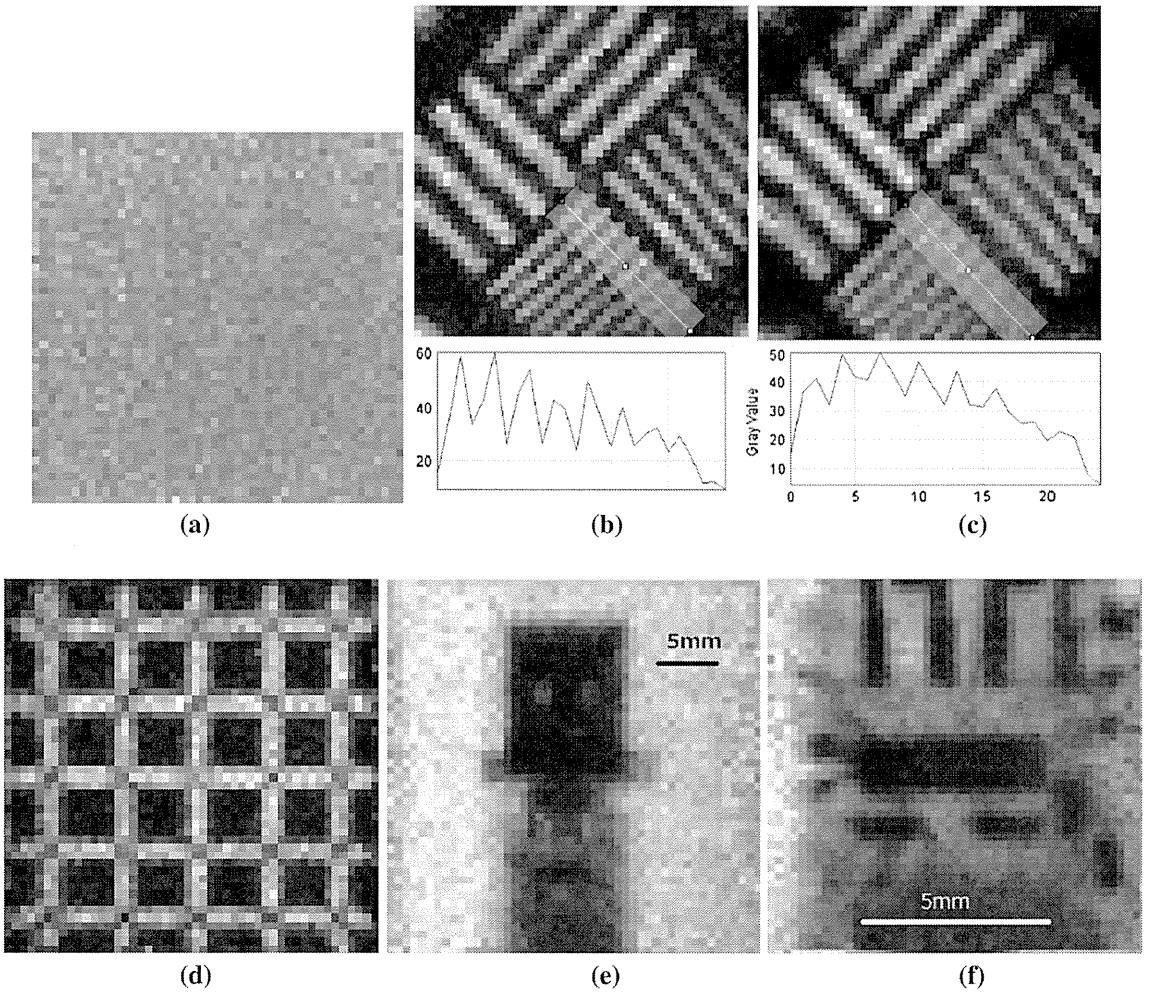

Fig. 5 Uniformity images (**a**), resolution phantom image, and profile measured with 122-keV gamma photons (**b**), measured with 35-keV gamma photons (**c**), linearity phantom image (**d**), transmission image of USB memory (**e**), and magnified transmission image of USB memory (**f**)

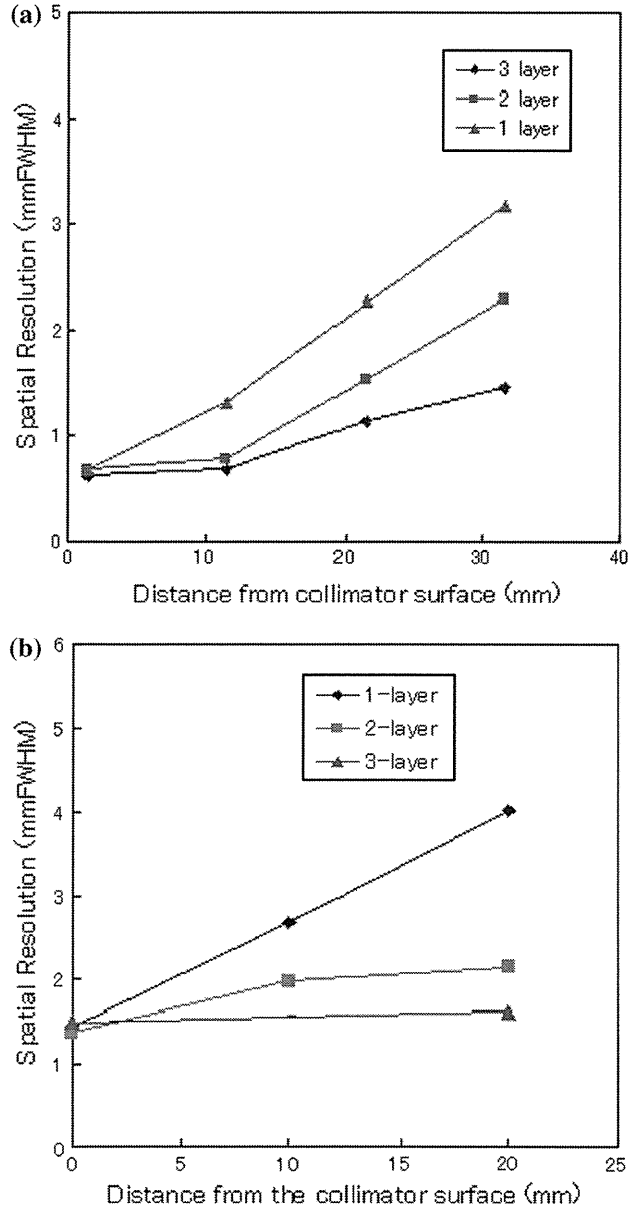

Fig. 6 System spatial resolution of YSO gamma camera system for 122-keV gamma photons (**a**) and 35-keV gamma photons (**b**)

phantom image is shown in Fig. 5d. No observable distortion can be seen in it.

We show the transmission images of a USB memory stick in Fig. 5e and a magnified transmission image in Fig. 5f. The magnifications of these images were ~0.7 and ~4, respectively. We observed metals and such electronics parts as an integrated circuit (IC) and capacities in the USB memory stick.

System spatial resolution

The spatial resolution with a parallel hole collimator 2 mm from the collimator surface was 0.7- and 1.3-mm FWHM for 122- (Fig. 6a) and ~35-keV (Fig. 6b) gamma photons, respectively.

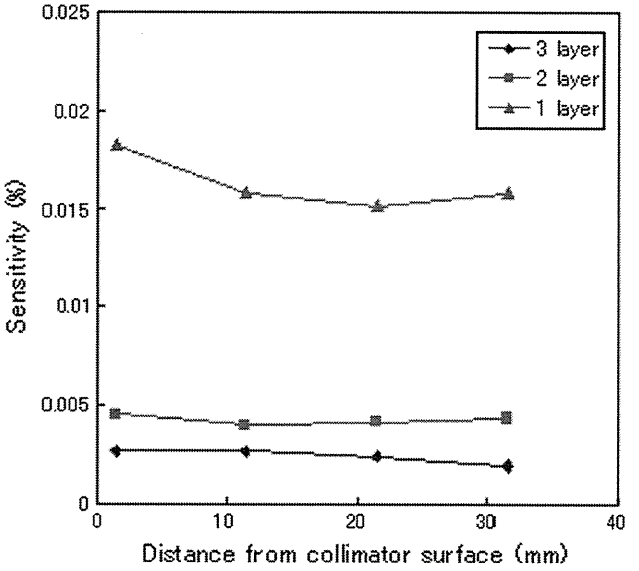

Fig. 7 Sensitivity of YSO gamma camera with parallel hole collimators

System sensitivity with collimators

The sensitivities of the YSO gamma camera with parallel hole collimators were ~0.0025 and ~0.016 % with three layers and one collimator layer, respectively (Fig. 7).

Small animal imaging

We show the whole body image of a rat to which Tc-99 m HMDP was administered in Fig. 8. We can observe such small bone structures as the spine.

Discussion

We developed a high-resolution YSO gamma camera system and imaged a high-resolution rat image with the camera. The main difference compared with a previously developed GSO gamma camera [12] is the small pixel size and the large matrix sizes of the YSO block. The previous camera used 1.9 × 1.9-mm GSO pixels, while ours used 0.8 × 0.8-mm YSO pixels. The matrix size of the previous one was 22 × 22, and we increased ours to 48 × 48. The pixels were less than halved, and the matrixes were more than doubled in both directions. The 0.8-mm scintillator pixels used for single-photon imaging system is probably smallest so far except for the prototype SiPM-based gamma camera system [14]. By such improvements (smaller and more pixels), the new gamma camera

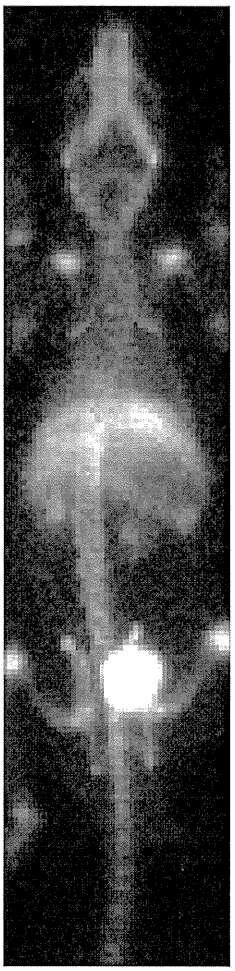

Fig. 8 Image of rat administered Tc-99 m MDP measured by YSO gamma camera

provided images with much higher resolution not only for phantoms, but also for rat than the previous one.

However, our presented system has a drawback. The sensitivity of the parallel hole collimator is roughly proportional to the area of a collimator hole. Since we used a one-to-one coupled parallel hole collimator, the sensitivity became lower for the collimator with a small hole. In fact, the sensitivity of the previously developed GSO gamma camera was ~0.05 % for a three-layer collimator, but the new one was ~0.0025 %, which decreased to a factor of ~20. The ratio of the area of the previously developed collimator hole to new one was ~10. Some of the discrepancies of the ratio could be attributed to the differences in the detection efficiency of the scintillators (YSO and GSO) and the packing fractions of these scintillators. To obtain images with identical total counts, the acquisition time or the radioactivity level must be increased. The previously developed GSO gamma camera still has advantages: high sensitivity and usefulness for low-dose experiments or those that need short acquisition times, such as dynamic studies.

The energy resolution of our developed YSO gamma camera was inferior to the previously developed GSO gamma camera. Our YSO gamma camera had energy resolution of ~20 % FWHM, but the GSO gamma camera's resolution was ~15 %, although the YSO light output was ~2.5 times higher than GSO. One possible explanation is that the YSO pixel was so small (0.8 × 0.8 mm) that the scintillation light was absorbed in the pixels. The depth dependency of the light output from the pixels also increases for these small pixels.

The main advantage of our YSO gamma camera is its high resolution and relatively low cost. This high-resolution YSO gamma camera may replace the NaI(Tl)-based small field-of-view (FOV) gamma cameras, which are sometimes used for small animal SPECT systems. The manufacturing cost of such non-hygroscopic scintillators as YSO is lower than that of such hygroscopic ones as NaI(Tl). The small pixels of this YSO gamma camera can reduce the size of the detector used for SPECT systems and reduce their cost. The YSO gamma camera also has the potential to overcome the drawbacks of CdTl- or CZT-based gamma cameras whose costs are relatively high. The PSPMT cost for the YSO gamma camera is also less, so a high-resolution gamma camera with relatively low cost can be realized with our presented YSO gamma camera.

The separation of the bar phantom imaged with 122-keV gamma photons was better than that with 35-keV gamma photons (Fig. 5b, c). This is because the intrinsic spatial resolution of gamma camera is better for high-energy gamma photons, because the higher-energy gamma photons produce higher scintillation light photons; thus the statistical deviation of position calculation is smaller, in a similar manner to the relation between energy resolution and gamma photon energy [4].

The system spatial resolution became worse as the distance from the collimator increased (Fig. 6). Also, the resolution degradation was smaller for multilayer collimators. These results were exactly as expected and well suited to the theory. The sensitivity with parallel hole collimator was almost constant as a function of the distance from the collimator surface (Fig. 7). This was well suited to the theory. Also, the sensitivity was decreased as the number of the collimator layer increased. This was also identical to the theory.

Our developed YSO gamma camera will also be useful for sentinel lymph node imaging systems [9] due to its high resolution and relatively low weight (2.6 kg for the detector part). By changing the number of collimators, the sensitivity and spatial resolution selection will be practical for clinical environments in which the dynamic range of the activity is relatively wide.

Conclusions

We successfully developed a high-resolution YSO gamma camera system that employs 0.8-mm pixels. A high-resolution system has a potential to be useful for molecular imaging research using small animals as well as other medical imaging applications.

References

1. Beekman FJ, von der Have F. The pinhole: gateway to ultra-high resolution three dimensional radionuclide imaging. Eur J Nucl Med Mol Imaging. 2007;34:151–61.
2. Aoi T, Zeniya T, Watabe H, Deloar HM, Matsuda T, Iida H. System design and development of a pinhole SPECT system for quantitative function imaging of small animals. Ann Nucl Med. 2006;20:245–51.
3. Vaissier PE, Goorden MC, Vastenhouw B, van der Have F, Ramakers RM, Beekman FJ. Fast spiral SPECT with stationary γ-cameras and focusing pinholes. J Nucl Med. 2012;53(8):1292–9.
4. Tanaka E, Hiramoto T, Nohara N. Scintillation cameras based on new position arithmetic. J Nucl Med. 1970;11(9):542–7.
5. Olcott PD, Habte F, Foudray AM, Levin CS. Performance characterization of a miniature, high sensitivity gamma ray camera. IEEE Trans Nucl Sci. 2007;54(5):1492–7.
6. Zeniya T, Watabe H, Aoi T, Kim KM, Teramoto N, Takeno T, Ohta Y, Hayashi T, Mashino H, Ota T, Yamamoto S, Iida H. Use of a compact pixellated gamma camera for small animal pinhole SPECT imaging. Ann Nucl Med. 2006;20(6):409–16.
7. Dahlbom M, MacDonald LR, Eriksson L, Paulus M, Andreaco M, Casey ME, Moyers C. Performance of a YSO/LSO phoswich detector for use in a PET/SPECT system. IEEE Trans Nucl Sci. 1997;44(3):1114–9.
8. Yamamoto S, Watabe H, Kato K, Hatazawa J. Performance comparison of high quantum efficiency and normal quantum efficiency photomultiplier tubes and position sensitive photomultiplier tubes for high resolution PET and SPECT detectors. Med Phys. 2012;39(11):6900–7.
9. Abe A, Takahashi N, Lee J, Oka T, Shizukuishi K, Kikuchi T, Inoue T, Jimbo M, Ryuo H, Bicke C. Performance evaluation of a hand-held, semiconductor (CdZnTe)-based gamma camera. Eur J Nucl Med Mol Imaging. 2003;30(6):805–11.
10. Kim H, Furenlid LR, Crawford MJ, Wilson DW, Barber HB, Peterson TE, Hunter WC, Liu Z, Woolfenden JM, Barrett HH. SemiSPECT: a small-animal single-photon emission computed tomography (SPECT) imager based on eight cadmium zinc telluride (CZT) detector arrays. Med Phys. 2006;33(2):465–74.
11. Ogawa K, Ohmura N, Iida H, Nakamura K, Nakahara T, Kubo A. Development of an ultra-high resolution SPECT system with a CdTe semiconductor detector. Ann Nucl Med. 2009;23(8):763–70.
12. Yamamoto S, Watabe H, Kanai Y, Shimosegawa E, Hatazawa J. Development of a pixelated GSO gamma camera system with tungsten parallel hole collimator for single photon imaging. Med Phys. 2012;39(2):581–8.
13. Yamamoto S, Imaizumi M, Shimosegawa E, Hatazawa J. Development of a compact and high spatial resolution gamma camera system using LaBr 3(Ce). Nucl Instrum Methods Phys Res Sec A. 2010;622(1):261–9.
14. Yamamoto S, Watabe H, Kanai Y, Imaizumi M, Watabe T, Shimosegawa E, Hatazawa J. Development of a high-resolution Si-PM-based gamma camera system. Phys Med Biol. 2011;56(239):7555–67.

JJCO Japanese Journal of Clinical Oncology

Japanese Journal of Clinical Oncology, 2015, 45(1) 12–18
doi: 10.1093/jjco/hyu160
Advance Access Publication Date: 20 October 2014
Original Article

OXFORD

Original Article

Phase I and pharmacokinetic study of trastuzumab emtansine in Japanese patients with HER2-positive metastatic breast cancer

Harukaze Yamamoto[1,2,*], Masashi Ando[3], Kenjiro Aogi[4], Hiroji Iwata[5], Kenji Tamura[1,2], Kan Yonemori[1], Chikako Shimizu[1], Fumikata Hara[4], Daisuke Takabatake[6], Masaya Hattori[5], Takashi Asakawa[7], and Yasuhiro Fujiwara[1]

[1]Department of Breast and Medical Oncology, National Cancer Center Hospital, Tokyo, [2]Department of Medical Oncology and Translational Research Graduate School of Medical Sciences, Kumamoto University, Kumamoto, [3]Department of Clinical Oncology, Aichi Cancer Center Hospital, Aichi, [4]Department of Breast Oncology, Shikoku Cancer Center, Ehime, [5]Department of Breast Oncology, Aichi Cancer Center Hospital, Aichi, [6]Department of Breast Surgery, Kochi Health Science Center, Kochi, and [7]Department of Clinical Research Planning, Chugai Pharmaceutical Co, Ltd, Tokyo, Japan

*For reprints and all correspondence: Harukaze Yamamoto, Department of Breast and Medical Oncology, National Cancer Center Hospital, 5-1-1 Tsukiji, Chuo-ku, Tokyo 104-0045, Japan. E-mail: haryamam@ncc.go.jp

Received 14 August 2014; Accepted 23 September 2014

Abstract

Objective: Trastuzumab emtansine (T-DM1), an antibody–drug conjugate composed of the cytotoxic agent DM1 conjugated to trastuzumab via a stable thioether linker, has shown clinical activity in human epidermal growth factor receptor 2-positive metastatic breast cancer patients. This study evaluated the maximum tolerated dose, toxicity and pharmacokinetics of trastuzumab emtansine in Japanese breast cancer patients.

Methods: Inoperable advanced or recurrent human epidermal growth factor receptor 2-positive breast cancer patients were administered trastuzumab emtansine intravenously at a dose of 1.8, 2.4 or 3.6 mg/kg every 3 weeks. The maximum tolerated dose was estimated using the continual reassessment method.

Results: This study enrolled 10 patients who were administered trastuzumab emtansine for a median of seven cycles. The dose-limiting toxicity was Grade 3 elevation of aspartate aminotransferase/alanine aminotransferase at the 2.4 mg/kg dose level. The maximum tolerated dose was estimated to be 3.6 mg/kg because at the point when dose-limiting toxicity was evaluable in 10 patients, the probability of dose-limiting toxicity estimated using the continual reassessment method was closest to 25% at a dose of 3.6 mg/kg and this was unchanged by the results for patients enrolled after that. The most frequent adverse events were nausea, arthralgia, fever, fatigue and decreased appetite. Adverse events were generally tolerable. The maximum concentration and area under the concentration–time curve increased linearly with the dose.

Conclusions: Trastuzumab emtansine up to 3.6 mg/kg was well tolerated by Japanese breast cancer patients. Although thrombocytopenia and hepatotoxicity tended to be more severe than was seen in